



# Clinopyroxene Dissolution Records Rapid Magma Ascent

David A. Neave<sup>1\*</sup> and John Maclennan<sup>2</sup>

<sup>1</sup> Department of Earth and Environmental Sciences, The University of Manchester, Manchester, United Kingdom,

<sup>2</sup> Department of Earth Sciences, University of Cambridge, Cambridge, United Kingdom

Magma ascent rates control volcanic eruption styles. However, the rates at which basaltic magmas ascend through the crust remain highly uncertain. Although recent studies have successfully exploited records of decompression driven degassing to estimate the rates at which H<sub>2</sub>O-rich basalts ascend, such approaches cannot readily be applied to primitive and H<sub>2</sub>O-poor basalts that erupt in ocean island and mid-ocean ridge settings. Here we present magma ascent rates obtained by modeling the dissolution of clinopyroxene crystals in a wehrlitic nodule from the primitive Borgarhraun lava flow in North Iceland. High-Al<sub>2</sub>O<sub>3</sub> clinopyroxene core compositions are consistent with crystallization near the Moho (~800 MPa), whereas low-Al<sub>2</sub>O<sub>3</sub> clinopyroxene rims and inclusion compositions are consistent with crystallization at or near the surface. We interpret low-Al<sub>2</sub>O<sub>3</sub> rims and inclusions as the crystallized remnants of boundary layers formed by the dissolution of high-Al<sub>2</sub>O<sub>3</sub> clinopyroxene during magma ascent. By combining characteristic rim dissolution lengths of 50–100 μm with published experimental calibrations of clinopyroxene dissolution behavior, we estimate that the Borgarhraun magma most likely decompressed and ascended at rates of 3.0–15 kPa.s<sup>-1</sup> and 0.11–0.53 m.s<sup>-1</sup>, respectively. These rates are slightly faster than published estimates obtained by modeling the diffusive re-equilibration of olivine crystals, suggesting that the Borgarhraun magma either accelerated upwards or that it stalled briefly at depth prior to final ascent. Comparisons with other basaltic eruptions indicate that the H<sub>2</sub>O-poor magma that fed the dominantly effusive Borgarhraun eruption ascended at a similar rate to some H<sub>2</sub>O-rich magmas that have fed explosive eruptions in arc settings. Thus, magma ascent rates do not appear to correlate simply with magma H<sub>2</sub>O contents. Overall, our findings confirm that primitive and H<sub>2</sub>O-poor basalts can traverse the crust within days, and may erupt with little precursory warning of magma ascent.

**Keywords:** magma ascent rate, plumbing system, clinopyroxene dissolution, basalt, disequilibrium, Iceland

## 1. INTRODUCTION

Volcanoes are underlain by vertically extensive and geometrically complex magmatic plumbing systems that are capable of dynamically reorganizing themselves over the timescales of individual eruptions (Marsh, 2004; Cashman et al., 2017; Sparks and Cashman, 2017; Magee et al., 2018; Maclennan, 2019; Sparks et al., 2019). It is therefore essential to quantify magma storage and transport timescales if we are to develop accurate models of volcanic behavior. Magma ascent rates

### OPEN ACCESS

#### Edited by:

Mattia Pistone,  
University of Georgia, United States

#### Reviewed by:

Silvio Mollo,  
Sapienza University of Rome, Italy  
Chiara Maria Petrone,  
Natural History Museum,  
United Kingdom

#### \*Correspondence:

David A. Neave  
david.neave@manchester.ac.uk

#### Specialty section:

This article was submitted to  
Petrology,  
a section of the journal  
Frontiers in Earth Science

Received: 09 March 2020

Accepted: 11 May 2020

Published: 10 June 2020

#### Citation:

Neave DA and Maclennan J (2020)  
Clinopyroxene Dissolution Records  
Rapid Magma Ascent.  
Front. Earth Sci. 8:188.  
doi: 10.3389/feart.2020.00188

are of particular importance in this respect because they play a central role in determining the style of volcanic eruptions, with eruptions fed by rapidly ascending magmas typically being more explosive than those fed by slowly ascending magmas (Gonnermann and Manga, 2007; Rutherford, 2008). Changes in magma ascent rate can also drive potentially hazardous transitions in eruption style (Woods and Koyaguchi, 1994). Importantly, global systematics in the eruptive behavior of volcanoes can now be resolved through the local complexity of individual events (Cassidy et al., 2018). However, most published estimates of magma ascent rate are from silicic systems despite the fact that basaltic systems are geographically widespread and dominate global magma budgets (Cassidy et al., 2018, and references therein). Although a number of studies have gone some way toward redressing this imbalance (e.g., Ruprecht and Plank, 2013; Lloyd et al., 2014; Peslier et al., 2015; Newcombe et al., 2020), estimates of magma ascent rate from basaltic systems remain few in number and somewhat uncertain in nature.

Magma ascent rates are commonly estimated using numerical modeling approaches of varying complexity (Wilson and Head, 1981; Mastin, 2002; La Spina et al., 2015, 2019). Analog modeling approaches have also been used to constrain magma ascent rates and inform the application of numerical models to natural systems (Namiki and Manga, 2006, 2008; Wright et al., 2012). However, ascent rates determined using modeling approaches are often subject to large uncertainties because conduit dimensions and eruptive mass fluxes are often very poorly constrained. Direct estimates of magma ascent rate have been obtained by modeling the diffusive re-equilibration of crystals entrained shortly before eruption (e.g., Ruprecht and Plank, 2013; Mollo et al., 2015; Mutch et al., 2019b; Newcombe et al., 2020), and the diffusive loss of volatiles from melt inclusions and melt embayments as a result of decompression-driven degassing (e.g., Humphreys et al., 2008; Lloyd et al., 2014; Hartley et al., 2018; Barth et al., 2019). Crystal textures have also been used to determine ascent rates in cases where crystallization kinetics are sufficiently well-understood (Armienti et al., 2013). However, ascent rates estimated from the re-equilibration of crystals, whether chemical or textural, convolve isobaric intervals of crystal entrainment with polybaric intervals of magma ascent, and are thus likely to underestimate true values. Although techniques that exploit decompression-driven volatile exsolution circumvent this particular problem, they can only be applied to magmas that degas significantly en route to the surface. Given that primitive basalts from ocean island and mid-ocean ridge settings often degas little during ascent because of their low volatile (i.e., H<sub>2</sub>O) contents (<0.2 wt.% H<sub>2</sub>O; Michael, 1988; Saal et al., 2002; Miller et al., 2019), the rates at which they ascend must be derived using different and volatile-independent approaches.

Basalts frequently carry crystals and nodules formed at depth to the surface, and exploiting the pressure-dependent stability of these crystalline cargoes provides a means of directly estimating the rates at which H<sub>2</sub>O-poor primitive basalts ascend (e.g., Brearley and Scarfe, 1986). Clinopyroxene is especially important in this regard because it commonly crystallizes from primitive basalts and its stability correlates strongly with pressure (Figure 1; Bender et al., 1978; Presnall et al., 1978;

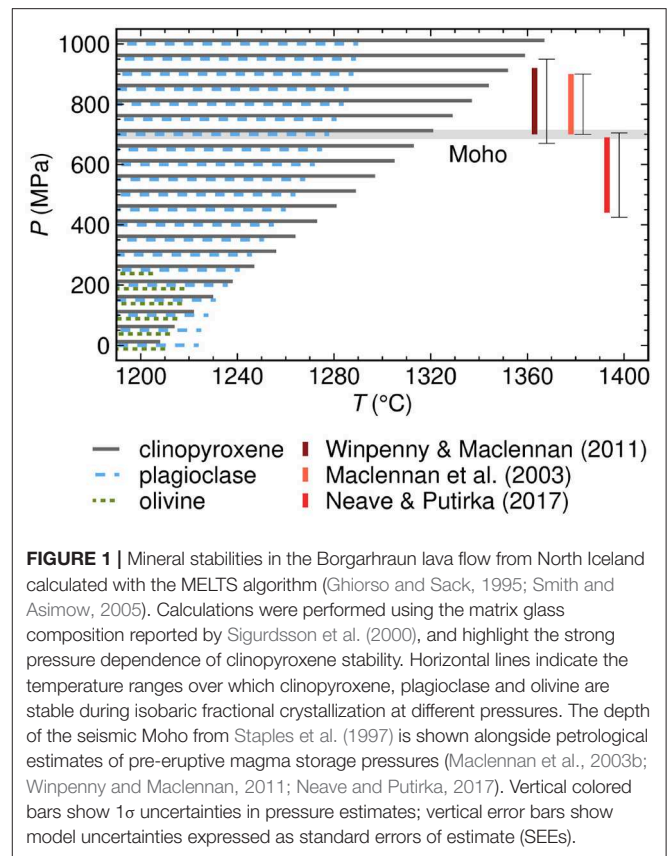


**FIGURE 1** | Mineral stabilities in the Borgarhraun lava flow from North Iceland calculated with the MELTS algorithm (Ghiorso and Sack, 1995; Smith and Asimow, 2005). Calculations were performed using the matrix glass composition reported by Sigurdsson et al. (2000), and highlight the strong pressure dependence of clinopyroxene stability. Horizontal lines indicate the temperature ranges over which clinopyroxene, plagioclase and olivine are stable during isobaric fractional crystallization at different pressures. The depth of the seismic Moho from Staples et al. (1997) is shown alongside petrological estimates of pre-eruptive magma storage pressures (MacLennan et al., 2003b; Winpenny and MacLennan, 2011; Neave and Putirka, 2017). Vertical colored bars show 1 $\sigma$  uncertainties in pressure estimates; vertical error bars show model uncertainties expressed as standard errors of estimate (SEEs).

Fujii and Bougault, 1983; Chen and Zhang, 2009; Holland et al., 2018). Clinopyroxene crystals formed at depth may therefore dissolve during ascent, as evidenced by the resorbed nature of phenocrystic and xenocrystic clinopyroxenes erupted from some basaltic volcanoes (e.g., Tsuchiyama, 1986; Gurenko and Sobolev, 2006; Eason and Sinton, 2009). Indeed, the dissolution of clinopyroxene crystals during magma ascent may be responsible for the pyroxene paradox whereby many mid-ocean ridge basalts preserve geochemical signals of clinopyroxene crystallization but contain no clinopyroxene crystals (O'Donnell and Presnall, 1980; Thompson et al., 1980; Grove et al., 1992).

Here we exploit a quantitative but little used description of clinopyroxene stability in basaltic magmas to estimate the rates at which primitive Icelandic basalts ascend through the crust. We do this by modeling the dissolution of clinopyroxene crystals in a wehrlitic nodule from the Borgarhraun lava flow in North Iceland. Our findings suggest that H<sub>2</sub>O-poor basalts from ocean island and mid-ocean ridge systems can ascend as fast as many of their H<sub>2</sub>O-rich counterparts from arc systems. This has important implications for evaluating risks posed by basaltic volcanoes as primitive magmas appear capable of traversing the whole crust within a few days.

## 2. NODULES IN ICELANDIC BASALTS

Basaltic magmas often carry nodules of crystalline material to the surface. These nodules provide crucial insights into

the chemical structure of Earth's interior and the dynamics of magmatic plumbing systems (e.g., Rudnick, 1992; Pearson et al., 2003; Holness et al., 2007; Cooper et al., 2016). Magmatic nodules occur in the products of numerous Icelandic eruptions and are variably wehrlitic, gabbroic, troctolitic and feldspathic in composition (Trønnes, 1990; Hansen and Grönvold, 2000; MacLennan et al., 2003a; Gurenko and Sobolev, 2006; Holness et al., 2007). Gabbroic, troctolitic and feldspathic nodules in lavas and tephra from the Eastern Rift Zone of Iceland are thought to constitute the disaggregated remnants of plagioclase-rich crystal mushes from the mid-crust (Hansen and Grönvold, 2000; Holness et al., 2007); macrocrysts and glomerocrysts of anorthitic plagioclase from the same samples are likewise considered to reflect more efficiently disaggregated portions of the same mushes (Halldórsson et al., 2008; Neave et al., 2014). In contrast, wehrlitic, gabbroic and troctolitic nodules from the Miðfell and Borgarhraun lava flows in the Western and Northern Volcanic Zones of Iceland, respectively, are thought to reflect the crystallization, mixing and reaction of primitive magmas in the lower crust and uppermost mantle (Trønnes, 1990; MacLennan et al., 2003a; Gurenko and Sobolev, 2006). Nodules from the Borgarhraun lava flow are of particular interest because of their extremely primitive compositions [olivine  $X_{\text{Fo}}$  up to 0.92, where  $X_{\text{Fo}}$  = molar Mg/(Mg+Fe); plagioclase  $X_{\text{An}}$  up to 0.92, where  $X_{\text{An}}$  = molar Ca/(Ca+Na); and clinopyroxene  $\text{Mg}_{\text{cpx}}$  up to 0.90, where  $\text{Mg}_{\text{cpx}}$  = Mg/(Mg+Fe)]. These crystals therefore preserve information about the earliest evolution of mantle-derived melts that would have otherwise been obscured by mixing and sampling bias (MacLennan, 2008; Winpenny and MacLennan, 2011; Neave et al., 2019b).

Nodules from the Borgarhraun lava flow are well-suited for estimating primitive basalt ascent rates because there are excellent geobarometric constraints on the pressure (i.e., depth) at which they were stored prior to eruption (**Figure 1**); the depth from which magma ascended is well-known. Clinopyroxene-liquid geobarometry using the model of Putirka et al. (1996) indicates that the Borgarhraun magma was stored at  $810 \pm 110(1\sigma)$  MPa in the uppermost mantle prior to eruption (Winpenny and MacLennan, 2011). The model uncertainty (standard error of estimate, SEE) associated with the geobarometer of Putirka et al. (1996) is 140 MPa. This pre-eruptive storage pressure is corroborated by experimental petrology and geobarometry exploiting the pressure dependence of olivine-plagioclase-augite-melt cotectic positions (Yang et al., 1996; MacLennan et al., 2003b, 2012). In contrast, clinopyroxene-liquid geobarometry using the model of Neave and Putirka (2017) suggests that the Borgarhraun magma was stored within the lower crust at a slightly lower pressure of  $570 \pm 120(1\sigma)$  MPa. This model is also associated with an SEE of 140 MPa. Despite this discrepancy in storage pressure estimates, which probably reflects the model of Neave and Putirka (2017) being optimized for lower pressures and more evolved compositions than those considered here, it is nevertheless clear that the Borgarhraun magma was stored near, and quite probably below, the Moho immediately before eruption.

A further advantage of investigating the Borgarhraun lava flow is that two recent studies into magma storage and ascent

timescales provide an excellent framework within which we can interpret our new observations (Mutch et al., 2019a,b). Specifically, Mutch et al. (2019a) exploited the diffusive re-equilibration of spinel chadacrysts within clinopyroxene oikocrysts from wehrlitic nodules to estimate deep magma residence times on the order of 1,000 years. Exploiting the diffusive re-equilibration of olivine macrocrysts in the rims of wehrlitic nodules then allowed Mutch et al. (2019b) to estimate transcrustal magma transport times on the order of 10 days that correspond to minimum magma ascent rates of  $0.02\text{--}0.1\text{ m.s}^{-1}$ .

Here we investigate a wehrlitic nodule in sample JM27 collected in July 1999 from the eastern edge of the Borgarhraun lava flow ( $65^{\circ}51.05'\text{N}$ ,  $16^{\circ}59.93'\text{W}$ ). Although nodules with variably dunitic, wehrlitic, gabbroic and troctolitic compositions have been described from the same location by MacLennan et al. (2003a), we focus on wehrlitic sample JM27 for three reasons: firstly, the abundance of clinopyroxene makes it possible to robustly constrain the minimum apparent dissolution lengths required to avoid dissolution time estimates being compromised by 3-D cutting effects; secondly, the presence of variably orientated crystals allows the effects of anisotropy on apparent dissolution lengths to be evaluated; and thirdly, the nodule's internal porosity likely prevented the dissipation of dissolution textures by convection or turbulent mingling. Nevertheless, we note that other nodules described by MacLennan et al. (2003a) show similar features to those we describe in sample JM27 (**Supplementary Material**), indicating that our findings are applicable to the Borgarhraun eruption as a whole.

### 3. METHODS

QEMSCAN imaging of sample JM27 was performed on a FEI Quanta-650F instrument in the Department of Earth Sciences at the University of Cambridge, UK. Images were collected with a  $4\text{-}\mu\text{m}$  pixel spacing, and 2000-count EDX spectra were used to produce phase and Al concentration maps following the principles discussed by Pirrie et al. (2004) and Neave et al. (2017a). Additional backscattered electron (BSE) imaging was performed on a FEI Quanta-650F instrument in the Department of Earth and Environmental Sciences at the University of Manchester, UK.

Mineral compositions were determined by electron probe microanalysis (EPMA) on a Cameca SX100 instrument in the Department of Earth Sciences at the University of Cambridge, UK. Silicon, Ti, Al, Cr, Fe, Mn, Mg, Ca, Na, K, and Ni were measured in minerals with an accelerating voltage of 15 kV. Olivine, clinopyroxene and spinel were measured with a current of 20 nA and a spot size of  $1\text{ }\mu\text{m}$ . Plagioclase was measured with a current of 10 nA and a spot size of  $5\text{ }\mu\text{m}$ . The following standards were used for calibration: diopside (Si and Ca), rutile (Ti), corundum (Al), Cr metal (Cr), fayalite (Fe), Mn metal (Mn), St. Johns olivine (Mg), jadeite (Na), orthoclase (K), and NiO (Ni). Peak and background counting times were typically 20 and 10 s, respectively for major elements and 40 and 20 s, respectively for minor elements, with the exception of Na that was counted on-peak for 10 s. Data quality was monitored by measuring

the following secondary standards (representative analyses are provided in the **Supplementary Material**): San Carlos olivine (NMNH 111312-44), Lake County plagioclase (NMNH 115900), Kakanui augite (NMNH 122142), and Ney County Cr-augite (NMNH 164905) (Jarosewich et al., 1980, 1987). Accuracy and precision are both estimated as  $\leq 1\%$  relative for major elements (present at  $>1$  wt.%) and  $\leq 5\%$  relative for minor elements (present at  $<1$  wt.%).

## 4. RESULTS

### 4.1. Petrography and QEMSCAN Imaging

The wehrlitic nodule in sample JM27 is composed of clinopyroxene with subordinate olivine and rare plagioclase (**Figures 2A, 3A; Supplementary Material**). Equant clinopyroxene crystals in the nodule are typically  $500\ \mu\text{m}$  to  $1\ \text{mm}$  in diameter, while equant olivine crystals are typically  $200\text{--}500\ \mu\text{m}$  in diameter. Rare tabular plagioclase crystals up to  $250\ \mu\text{m}$  in length also occur. The nodule hosts a network of microcrystalline pockets and embayments of groundmass that are contiguous with the host lava groundmass (**Figure 3B**). These pockets and channels are sometimes vesiculated, indicating that the nodule was porous to its host lava prior to lava flow emplacement. Both lava and nodule groundmasses are composed of high-aspect-ratio plagioclase crystals intergrown with small crystals of olivine, clinopyroxene and ilmenite (**Figure 3B**). The boundary between the wehrlitic nodule and the groundmass—defined by the limit of connected clinopyroxene crystals—is highly sinuous (**Figure 2A**). Crystals of olivine, plagioclase and clinopyroxene occur outside the nodule both as individual macrocrysts and as macrocrysts within monomineralic and polymineralic glomerocrysts (**Figures 2A, 3D**). Typical macrocrystic and glomerocrystic crystal diameters span the following ranges:  $200\ \mu\text{m}$  to  $2\ \text{mm}$  for olivine;  $200\text{--}800\ \mu\text{m}$  for plagioclase; and  $200\text{--}800\ \mu\text{m}$  for clinopyroxene. Glomerocrystic plagioclase and clinopyroxene crystals often occur in ophitic arrangements (**Figure 3D**).

QEMSCAN phase maps highlight abundant plagioclase inclusions within the cores of nodule clinopyroxene crystals that have not been described in previous studies (**Figure 2B**). These plagioclase inclusions are typically  $20\text{--}100\ \mu\text{m}$  in length and irregular to vermicular in form (**Figure 3A**). Many plagioclase inclusions are associated with small ( $10\text{--}50\ \mu\text{m}$ ) and irregular pockets of mesostasis that are texturally distinct from spheroidal melt inclusions (**Figure 3C**). Numerous small crystals of plagioclase also occur within the rims of nodule clinopyroxene crystals. Some of these crystals are separated from the groundmass by their host crystals and represent true inclusions. Others form continuous chains of crystals that extend from clinopyroxene rims deep into the interior of clinopyroxene cores. Within the limited compositional resolution of QEMSCAN phase identification, plagioclase inclusions have similar compositions to groundmass plagioclase crystals (bytownitic to labradoritic), while plagioclase macrocrysts and nodule plagioclase crystals are more primitive (anorthitic to bytownitic).

Semi-quantitative Al concentration maps indicate that plagioclase inclusions are located within domains of low- $\text{Al}_2\text{O}_3$

clinopyroxene that also appear to form inclusions within high- $\text{Al}_2\text{O}_3$  clinopyroxene cores (**Figure 2C**). Note that we refer to these low- $\text{Al}_2\text{O}_3$  clinopyroxene domains as inclusions without implying any genetic connotations. In other words, low- $\text{Al}_2\text{O}_3$  clinopyroxene inclusions are simply considered as domains of low- $\text{Al}_2\text{O}_3$  clinopyroxene that appear to be enclosed by high- $\text{Al}_2\text{O}_3$  clinopyroxene. Importantly, the presence and nature of these low- $\text{Al}_2\text{O}_3$  clinopyroxene inclusions was only revealed through Al concentration mapping; variations in clinopyroxene  $\text{Al}_2\text{O}_3$  content were not apparent during optical microscopy or phase mapping. Nodule clinopyroxene rims have similarly low  $\text{Al}_2\text{O}_3$  contents to clinopyroxene inclusions. Indeed, the chains of plagioclase crystals described in the preceding paragraph lie within low- $\text{Al}_2\text{O}_3$  channels that extend from clinopyroxene rims deep into their cores. Low- $\text{Al}_2\text{O}_3$  clinopyroxene inclusions are on the order of  $50\text{--}250\ \mu\text{m}$  in diameter, while the thinnest nodule clinopyroxene rims—those least affected by sectioning effects—are  $50\text{--}100\ \mu\text{m}$  wide.

High- $\text{Al}_2\text{O}_3$  clinopyroxene cores have relatively low BSE intensities while low- $\text{Al}_2\text{O}_3$  clinopyroxene rims and inclusions have relatively high BSE intensities (**Figures 3A,B**). Boundaries between nodule clinopyroxene cores and rims are often rounded (**Figure 3B**). As previously documented by Winpenny and MacLennan (2011), subtle variations in BSE intensity within nodule clinopyroxene cores delimit sector zones. Patchy variations in BSE intensity also occur at the edges of some clinopyroxene inclusions (**Figure 3A**), but appear to represent complex interfaces between inclusions and their host crystals rather than zoning intrinsic to low- $\text{Al}_2\text{O}_3$  clinopyroxene inclusions (**Figures 3B,C**). Importantly, we see no crystallographically controlled variations in BSE intensity that would reveal the presence of exsolution lamellae within nodule clinopyroxene cores (e.g., Holness et al., 2011).

Although BSE intensity is broadly constant within low- $\text{Al}_2\text{O}_3$  clinopyroxene inclusions, some inclusions contain films and pockets of very high BSE intensity (**Figure 3C**). These films and pockets typically occur next to plagioclase inclusions and along the inclusions' boundaries with high- $\text{Al}_2\text{O}_3$  clinopyroxene hosts, suggesting that they represent domains of late-stage crystallization. Further evidence for late-stage crystallization is provided by the small oxide crystals ( $5\text{--}20\ \mu\text{m}$  in diameter, and subsequently identified as titanomagnetite) that occur along some interfaces between plagioclase inclusions and portions of clinopyroxene inclusions with very high BSE intensities (**Figure 3C**).

### 4.2. Electron Probe Microanalysis

Plagioclase and olivine compositions from sample JM27 are summarized in **Figure 4**. Plagioclase compositions range from  $X_{\text{An}} = 0.70$  to  $X_{\text{An}} = 0.91$  (**Figure 4A**), and different compositions are found in different textural associations. High  $X_{\text{An}}$  contents ( $>0.85$ ) are only found in rare nodule plagioclase cores and the cores of some macrocrysts and glomerocrysts. Moderate  $X_{\text{An}}$  contents ( $0.78\text{--}0.85$ ) are found in nodule plagioclase rims, some plagioclase inclusions and in the cores and rims of some macrocrysts and glomerocrysts. Low  $X_{\text{An}}$  contents ( $<0.78$ ) are found in some plagioclase inclusions

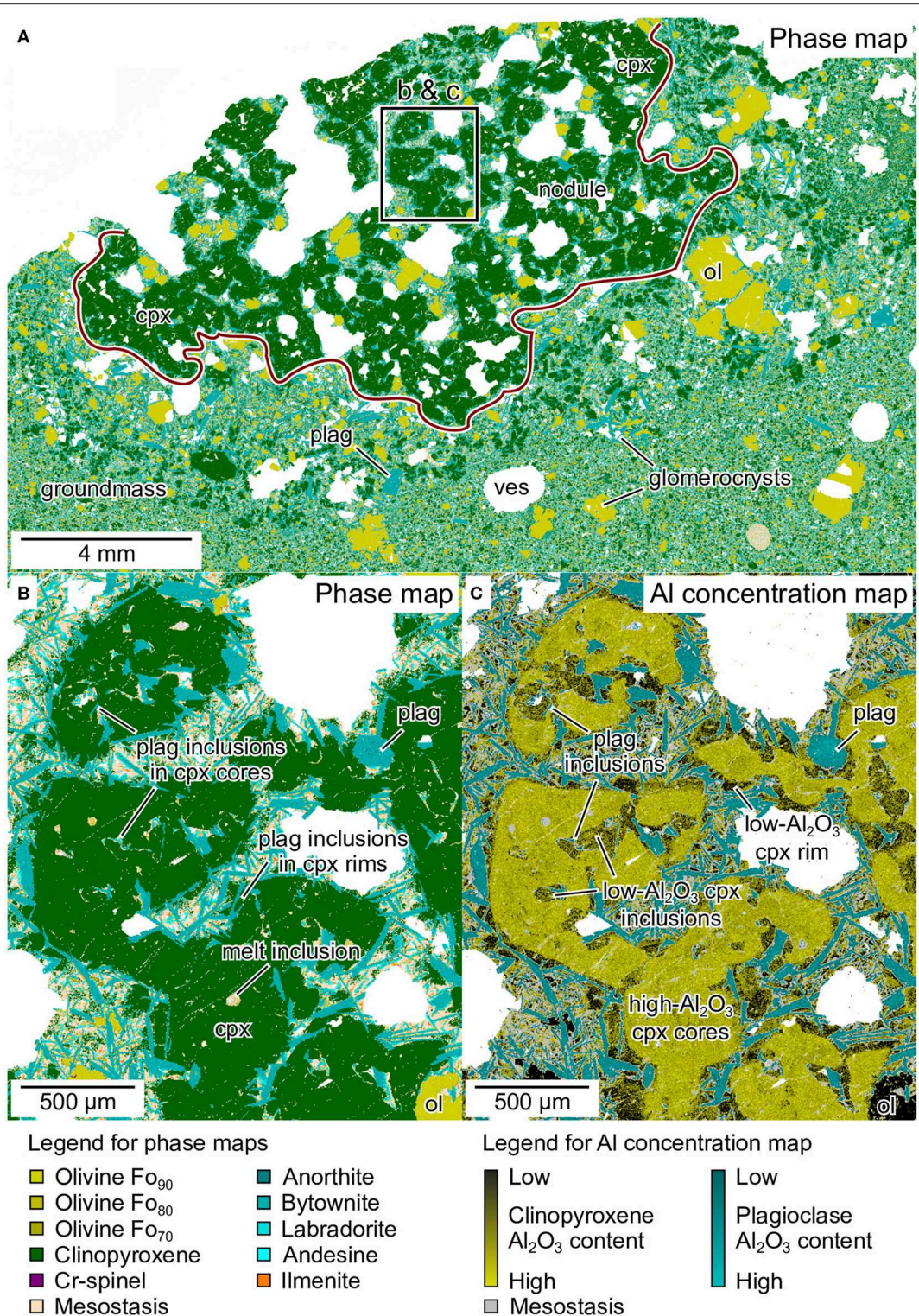


**FIGURE 2 |** Phase and Al concentration maps of a wehrlitic nodule in sample JM27 from the Borgarhraun lava flow in North Iceland obtained by QEMSCAN. **(A)** The wehrlitic nodule is composed of clinopyroxene with subordinate olivine and rare plagioclase. It also contains pockets and channels of crystalline groundmass that are contiguous with the lava groundmass, indicating that the nodule was porous at the point of lava flow emplacement. Macrocrystic and glomerocrystic olivine, plagioclase and clinopyroxene also occur in the lava groundmass. **(B)** Plagioclase inclusions are present in the cores and rims of clinopyroxenes in the wehrlitic nodule. **(C)** Clinopyroxene cores in the wehrlitic nodule have relatively high Al<sub>2</sub>O<sub>3</sub> contents, whereas clinopyroxene rims have relatively low Al<sub>2</sub>O<sub>3</sub> contents. Plagioclase inclusions in clinopyroxene cores are associated with inclusions of low-Al<sub>2</sub>O<sub>3</sub> clinopyroxene that are not evident in phase maps.

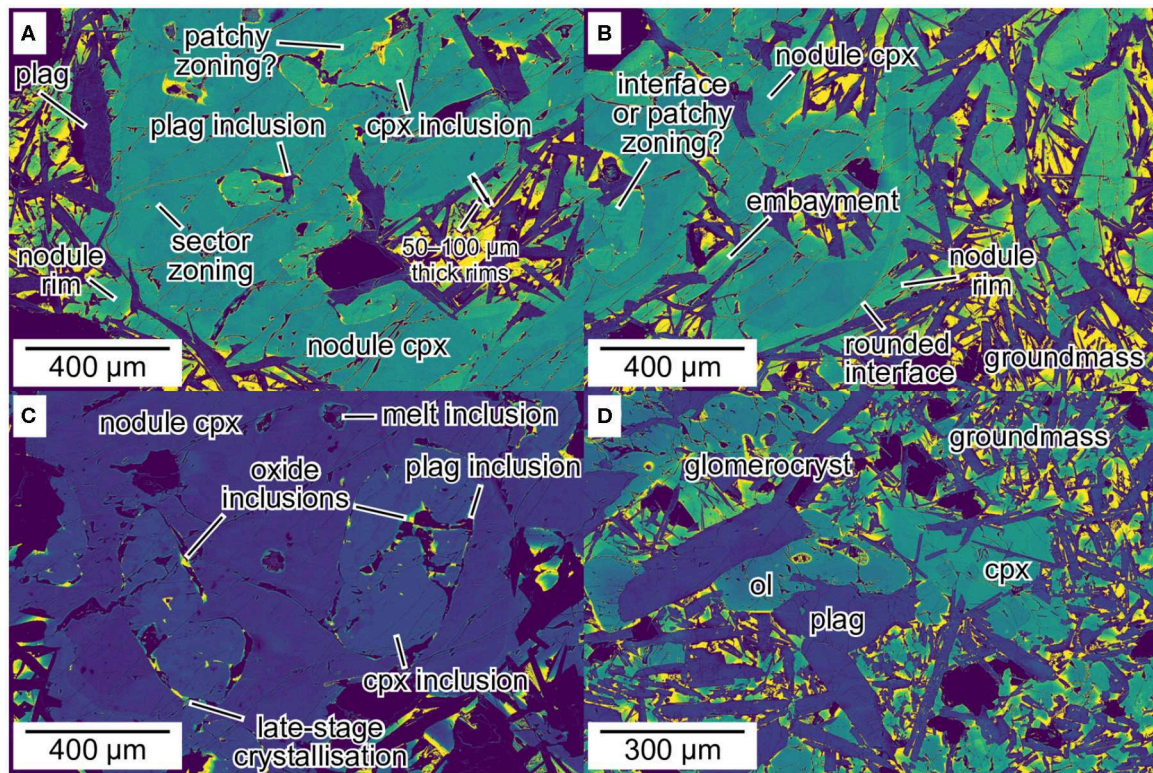
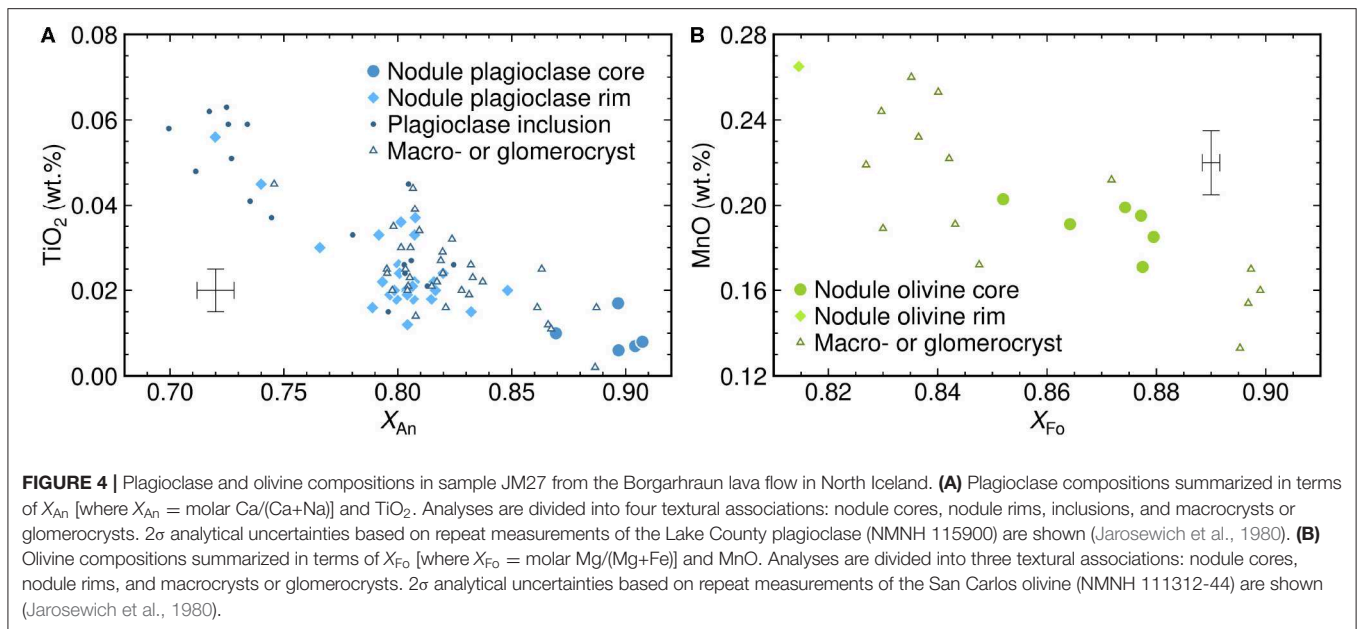


**FIGURE 3** | Backscattered electron (BSE) images of mineral textures in sample JM27 from the Borgarhraun lava flow in North Iceland. Raw and additional representative images are provided in the **Supplementary Material**. **(A,B)** Nodule clinopyroxene cores have low but variable BSE intensities consistent with the presence of sector zoning. Nodule clinopyroxene rims and inclusions have slightly higher BSE intensities that increase greatly toward the groundmass and pockets of late-stage crystallization respectively. Nodule clinopyroxene rims and inclusions both contain irregular plagioclase inclusions. **(C)** Pockets of late-stage crystallization within clinopyroxene inclusions have very high BSE intensities and are associated with both plagioclase and oxide (titanomagnetite) inclusions. **(D)** Macrocrystic and glomerocrystic olivine, plagioclase and clinopyroxene occur in the crystalline lava groundmass. Plagioclase macrocrysts and glomerocrysts are typically larger than plagioclase crystals in the wehrlitic nodule. Clinopyroxene macrocrysts and glomerocrysts are often arranged in ophitic arrangements with plagioclase.

and the outermost rims of macrocrysts, glomerocrysts and nodule plagioclase crystals. These low  $X_{An}$  contents are typically located close to films and pockets of late-stage crystallization (**Figure 3C**). Olivine compositions range from  $X_{Fo} = 0.81$  to  $X_{Fo} = 0.90$  (**Figure 4B**). Relationships between composition and texture are less clear for olivine than plagioclase, though nodule, macrocryst, and glomerocryst olivine cores typically contain the highest  $X_{Fo}$  contents ( $>0.85$ ). Lower  $X_{Fo}$  contents (0.82–0.85) are found in the cores and rims of some macrocrysts and glomerocrysts, and the lowest  $X_{Fo}$  content measured (0.81) is from a nodule olivine rim in contact with the groundmass.

Clinopyroxene compositions are summarized in **Figures 5, 6**, and range from  $Mg\#_{cpx} = 0.35$  to  $Mg\#_{cpx} = 0.91$ , with the majority of compositions lying between  $Mg\#_{cpx} = 0.85$  and  $Mg\#_{cpx} = 0.90$ . Different clinopyroxene compositions are closely linked with different textural associations. Nodule clinopyroxene cores are primitive ( $Mg\#_{cpx} = 0.88–0.91$ ; **Figures 5, 6**) and rich in octahedral Al ( $Al_{vi} = 0.08–0.11$ , where  $Al_{vi}$  is calculated on a six-oxygen basis; **Figure 6A**). They are also somewhat enriched in jadeite component [ $X_{Jd} = 0.012–0.018$ , where  $X_{Jd}$  is calculated following Putirka (2008);

**Figure 6B**]. Variability in  $TiO_2$  (0.11–0.20 wt.%; **Figure 5B**),  $Al_2O_3$  (4.0–5.5 wt.%; **Figure 5D**) and wollastonite component [ $X_{Wo} = 0.41–0.44$ , where  $X_{Wo} = Ca/(Ca+Mg+Fe)$  on a molar basis; **Figure 5F**] over the range of  $Mg\#_{cpx}$  contents present in nodule clinopyroxene cores reflects sector zoning (**Figure 3A**). Some macrocryst and glomerocryst cores have similar compositions to nodule clinopyroxene cores (i.e.,  $Mg\#_{cpx} = 0.88–0.90$  and  $Al_{vi} = 0.09–0.11$ ), while others are slightly more evolved. Nodule clinopyroxene rims are consistently more evolved than nodule clinopyroxene cores ( $Mg\#_{cpx} = 0.72–0.88$ ), a feature highlighted by the positive correlation between  $Mg\#_{cpx}$  and  $TiO_2$  defined by analyses from nodule clinopyroxene rims (**Figure 5B**). Rims are also considerably poorer in  $Al_{vi}$  ( $<0.08$ ; **Figure 6A**) and slightly poorer in  $X_{Jd}$  ( $<0.014$ ; **Figure 6B**) than nodule clinopyroxene cores. Some macrocryst and glomerocryst compositions overlap with nodule clinopyroxene compositions, though a few analyses extend to much more evolved compositions ( $Mg\#_{cpx}$  reaches as low as 0.55 and  $TiO_2$  reaches as high as 1.0 wt.%), probably reflecting late-stage crystallization during lava flow emplacement.



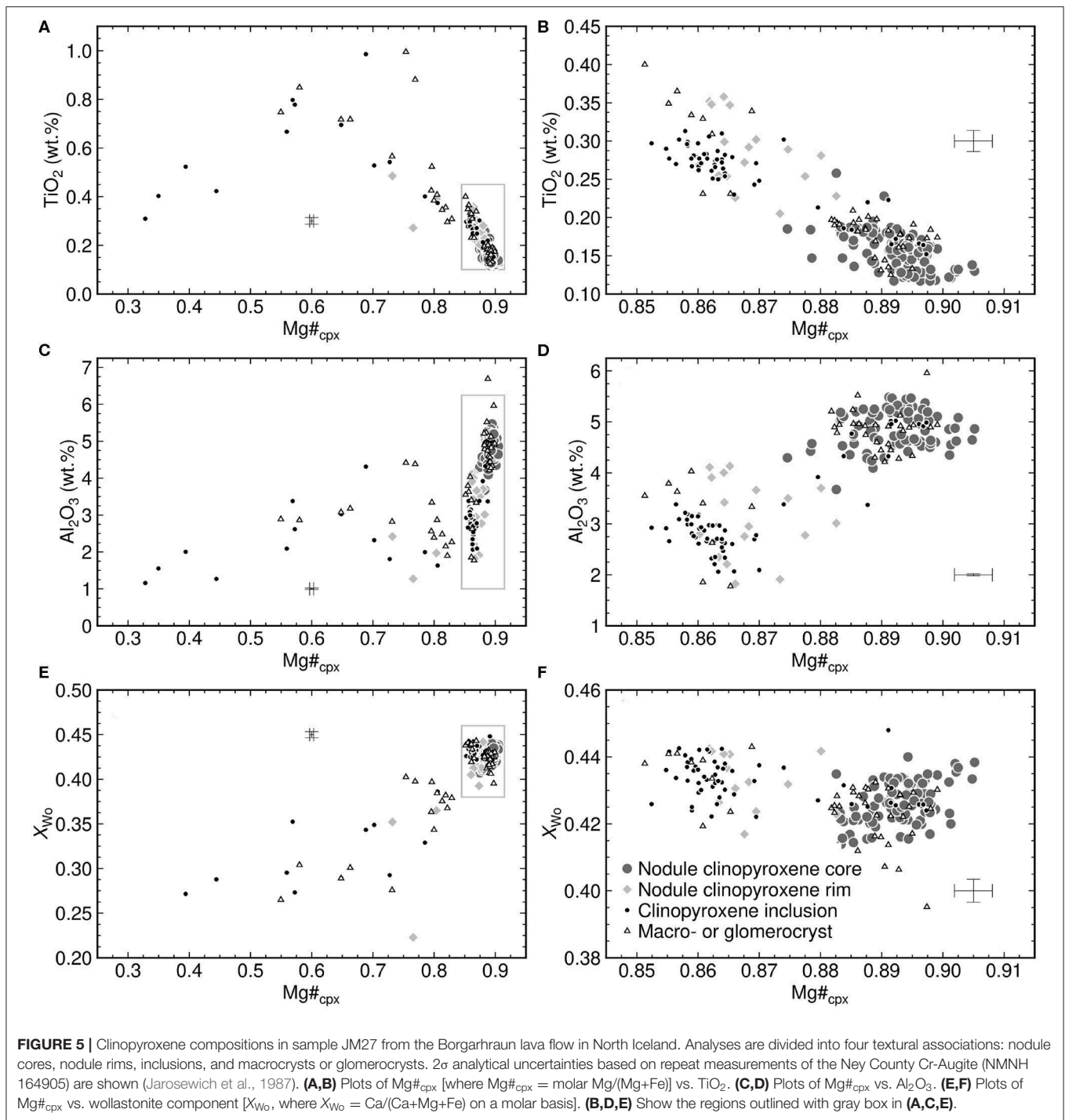
Clinopyroxene inclusions are the most compositionally variable of all clinopyroxene textural types ( $Mg\#_{cpx} = 0.35\text{--}0.90$ ). The majority of inclusion analyses fall within a compositional range shared with some macrocryst and glomerocryst analyses, as well as with analyses from nodule clinopyroxene rims ( $Mg\#_{cpx} = 0.85\text{--}0.87$ ,  $Al_2O_3 = 2.0\text{--}3.0$  wt.% and  $Al_{vi} = 0.03\text{--}0.06$ ; **Figures 5B,D, 6A**). These analyses are located within constant-BSE-intensity domains of clinopyroxene inclusions (**Figure 3A**). A primitive subpopulation of analyses from patchy zones at inclusion edges overlaps with analyses from nodule clinopyroxene core compositions ( $Mg\#_{cpx} = 0.88\text{--}0.90$ ,  $Al_2O_3 = 4.5\text{--}5.0$  wt.% and  $Al_{vi} = 0.08\text{--}0.09$ ), and probably constitutes analyses of complex, folded interfaces between inclusions and nodule clinopyroxene cores (**Figure 3B**). An evolved subpopulation of inclusion analyses overlaps partly with analyses from nodule clinopyroxene rims. These analyses are located within domains of very high BSE intensity that we have interpreted as pockets of late-stage crystallization (**Figure 3C**). The inflection of  $TiO_2$  content with decreasing  $Mg\#_{cpx}$  within this subpopulation reflects the onset of titanomagnetite crystallization.

## 5. IDENTIFYING CLINOPYROXENE DISSOLUTION

High- $Mg\#$  clinopyroxene crystals in the Borgarhraun lava flow record high pre-eruptive magma storage pressures of 570–810 MPa (Winpenny and MacLennan, 2011; Neave and Putirka, 2017). These pressures are consistent with the high  $Al_2O_3$ ,  $Al_{vi}$ , and  $X_{Jd}$  contents of macrocryst, glomerocryst, and nodule clinopyroxene cores investigated here, confirming the ultimately deep origin of sample JM27 (**Figures 3, 5B,C, 6**; Aoki and Kushiro, 1968; Thompson, 1974; Blundy et al., 1995;

Putirka et al., 1996). Given that the liquidus temperature of clinopyroxene is significantly higher at 570–810 MPa than 1 atm in Borgarhraun-like magmas [90–140°C higher according to calculations with the MELTS algorithm (**Figure 1**; Ghiorso and Sack, 1995; Smith and Asimow, 2005), and 70–120°C higher according to calculations on a compositionally analogous basalt from the Reykjanes Peninsula with THERMOCALC (RE46; Yang et al., 1996; Holland et al., 2018)], clinopyroxene crystals formed near the Moho are thus unlikely to have been in equilibrium with their carrier liquids upon eruption. Assuming that the ascending Borgarhraun magma cooled along an adiabatic gradient of  $<1^\circ C.km^{-1}$  (Katz et al., 2003), it thus seems probable that deep-formed high- $Al_2O_3$  clinopyroxene crystals would have at least partly dissolved en route to the surface.

The rounded nature of high- $Al_2O_3$ , high- $Al_{vi}$ , and high- $X_{Jd}$  nodule clinopyroxene cores indicates that they underwent dissolution prior to their encapsulation within low- $Al_2O_3$ , low- $Al_{vi}$ , and low- $X_{Jd}$  rims at or near the surface (**Figures 3B, 5B,C, 6**; Aoki and Kushiro, 1968; Thompson, 1974; Blundy et al., 1995; Putirka et al., 1996). A low-pressure origin for clinopyroxene rims is indicated by comparisons with the products of 1-atm experiments performed by Yang et al. (1996), as well as by clinopyroxene-liquid geobarometry performed on nodule clinopyroxene rims using the model of Neave and Putirka (2017). Geobarometry was undertaken on clinopyroxene rims using the matrix glass composition of Sigurdsson et al. (2000), and returned a pressure of  $210 \pm 35(1\sigma)$  MPa with an associated model SEE of 140 MPa. All clinopyroxene-liquid pairs were checked for multicomponent equilibrium following the approach of Neave et al. (2019a). Although 210 MPa is appreciably greater than 1 atm, it is, model uncertainties notwithstanding, considerably lower than the 570–810 MPa range obtained from high- $Al_2O_3$  cores (**Figure 1**; Winpenny and MacLennan, 2011; Neave and Putirka, 2017). Moreover, that only

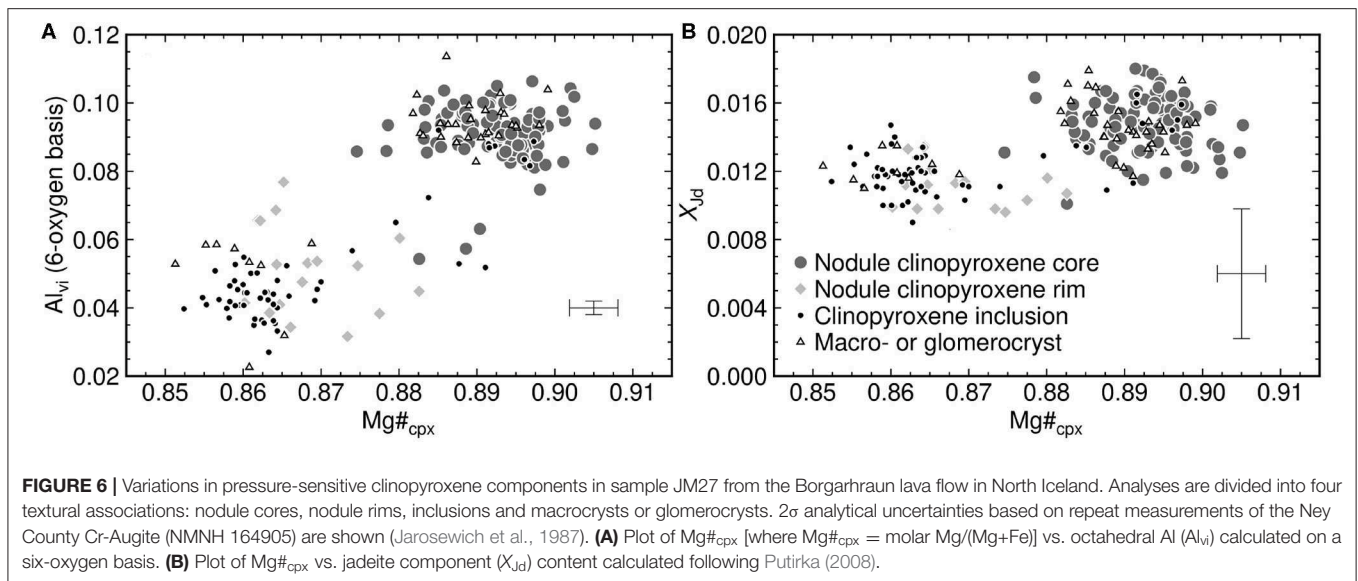


a few analyses passed equilibrium filters ( $n = 3$ ) suggests that clinopyroxene rims crystallized under disequilibrium conditions, feasibly resulting in an overestimation of crystallization pressures (Mollo et al., 2010).

The presence of abundant low- $Al_2O_3$  clinopyroxene inclusions within high- $Al_2O_3$  nodule clinopyroxene cores implies that dissolution was not only restricted to crystal faces, but also permeated crystal cores (Figure 3A). Similar

textures have been described in clinopyroxene macrocrysts from Haleakala volcano in Hawaii by Welsch et al. (2016), but were attributed to rapid, kinetically controlled crystal growth rather than dissolution. These authors came to this interpretation because both low- $Al_2O_3$  and high- $Al_2O_3$  domains of clinopyroxene macrocrysts are in contact with the groundmass in their samples, indicating that low- and high- $Al_2O_3$  clinopyroxene grew concurrently. However, only





low- $Al_2O_3$  rims are in contact the groundmass in sample JM27, ruling out concurrent growth in our case. Low- $Al_2O_3$  clinopyroxene inclusions in the Borgarhraun lava flow also cut across boundaries between sector zones within high- $Al_2O_3$  nodule clinopyroxene cores, demonstrating that the inclusions formed by the resorption of pre-existing crystal cores. The occurrence of low- $Al_2O_3$  clinopyroxene embayments within high- $Al_2O_3$  cores also suggests that clinopyroxene inclusions may represent ramifying networks of low- $Al_2O_3$  clinopyroxene channels in 3-D rather than isolated inclusions of the kind visible in 2-D. Indeed, the compositional similarity between clinopyroxene inclusions and nodule clinopyroxene rims suggests that they share a common dissolution-precipitation origin that we discuss in detail below (Figure 5). Finally, domains of patchy zoning associated with complex interface geometries between inclusions and their host crystals are similar to cellular dissolution textures in other systems (Figure 3B; Streck, 2008), highlighting dissolution's central role in clinopyroxene inclusion genesis.

Our observations from the Borgarhraun lava flow are not unique; similar observations from lavas erupted elsewhere in Iceland validate our identification of substantial clinopyroxene dissolution. For example, Trønnes (1990) and Hansteen (1991) described resorbed “Al- and Cr-rich endiopside” crystals equivalent to our nodule clinopyroxene cores in primitive basalts from the Hengill volcanic system in the Western Rift Zone. Gurenko and Sobolev (2006) also describe spongy and embayed high- $Al_2O_3$  clinopyroxene crystals in glass-hosted nodules from the primitive Miðfell lava flow, also from the Hengill volcanic system, though these authors account for dissolution by melt-rock reaction rather than decompression during ascent. Clinopyroxene dissolution has also been proposed as an explanation for the chemical systematics of lavas from both the Eastern and Western Rift Zones (Halldórsson et al., 2008; Eason and Sinton, 2009), illustrating its potentially widespread role in basalt petrogenesis.

In contrast with the glassy nodules from the Miðfell lava flow described by Gurenko and Sobolev (2006), the wehrlitic

nodule we describe here is fully crystalline; gabbroic and troctolitic nodules collected from the same location are similarly crystalline (Supplementary Material). Thus, while previously studied clinopyroxenes from the Miðfell lava flow are surrounded by glass, those we have studied from the Borgarhraun lava flow are surrounded by low- $Al_2O_3$  clinopyroxene rims. They are also permeated by low- $Al_2O_3$  clinopyroxene inclusions that host inclusions of relatively low- $X_{An}$  plagioclase. This important textural difference—the presence or absence of low- $Al_2O_3$  clinopyroxene around and within high- $Al_2O_3$  clinopyroxene cores—reflects the contrasting emplacement histories of the Miðfell and Borgarhraun lava flows. Specifically, the Miðfell lava flow was erupted subglacially, making it possible for Gurenko and Sobolev (2006) to collect glassy material from rapidly quenched pillow basalt rims. In contrast, the Borgarhraun lava flow erupted subaerially, meaning that sample JM27 cooled slowly and crystallized *in situ*. The relatively slow cooling of the Borgarhraun lava flow did however allow important information about the extent of pre-eruptive high- $Al_2O_3$  dissolution to be captured. Namely, low- $Al_2O_3$  clinopyroxene rims and inclusions record the approximate dimensions of boundary layers formed by the dissolution of high- $Al_2O_3$  clinopyroxene during magma ascent which were then preserved during cooling by the high closure temperature of major element diffusion within clinopyroxene (Freer et al., 1982).

Fractional crystallization calculations performed on the mean composition of high- $Al_2O_3$  nodule clinopyroxene cores with the MELTS algorithm at 1 atm reproduce the phase assemblage and phase proportions observed in clinopyroxene rims and inclusions (Ghiorso and Sack, 1995; Smith and Asimow, 2005). Crystallization was assumed to be fractional because lava flow cooling rates probably outpaced mineral-mineral equilibration rates. Olivine crystallization was also suppressed in favor of epitactic clinopyroxene growth. Calculations were performed without imposing oxygen fugacity constraints; oxygen fugacity was imposed from the starting clinopyroxene  $Fe^{2+}/Fe^{3+}$  estimated by charge balance following Lindsley and Andersen (1983). Once the calculated mass fraction of melt ( $F$ ) reached

0.05, calculated mass fractions of clinopyroxene, plagioclase and spinel-structured oxide were 0.89, 0.05, and 0.01, respectively, broadly in line with BSE observations from clinopyroxene inclusions (Figures 3A,C). Melts with the mean composition of high- $\text{Al}_2\text{O}_3$  nodule clinopyroxene cores thus crystallize clinopyroxene and plagioclase in a ratio of  $\sim 18:1$ , a ratio much closer to that observed in clinopyroxene inclusions than the  $\sim 1:1$  ratio calculated to result from matrix glass crystallization at 1 atm (Figures 3A,B). Moreover, pigeonite was predicted to crystallize at  $F < 0.12$ , consistent with the low  $X_{\text{W}_o}$  content of low- $\text{Mg}\#_{\text{cpx}}$  analyses from rims and inclusions associated with pockets of late-stage crystallization (Figures 3C, 5E).

Despite calculations with the MELTS algorithm reproducing the phase assemblage and phase proportions observed in clinopyroxene inclusions, they nevertheless return consistently higher  $\text{Mg}\#_{\text{cpx}}$  and  $X_{\text{An}}$  than observed in sample JM27 ( $\text{Mg}\#_{\text{cpx}} > 0.9$  until  $F < 0.25$  and  $X_{\text{An}} > 0.8$  until  $F < 0.15$ ). Although discrepancies between calculations with the MELTS algorithm and observations from both natural and experimental systems are well-documented (e.g., Neave et al., 2019b), they are probably exacerbated in this case by differences between the mean composition of high- $\text{Al}_2\text{O}_3$  nodule clinopyroxene cores and the compositions for which the MELTS algorithm has been calibrated (Ghiorso and Sack, 1995). However, a more fundamental explanation for these discrepancies stems from assuming that the boundary layers created by clinopyroxene dissolution were closed and compositionally homogeneous systems for their entire lifespans. Although these assumptions make performing illustrative calculations with the MELTS algorithm tractable, they are incorrect in detail. This is because our observations suggest Mg-rich and Na-poor high- $\text{Al}_2\text{O}_3$  clinopyroxene cannot be mass balanced against a Mg-poor and Na-rich assemblage containing low- $\text{Al}_2\text{O}_3$  clinopyroxene, plagioclase and titanomagnetite.

The dissolution rate of crystals is strongly controlled by the diffusivity of their constituent components in their surrounding melts, which results in the creation of concentration gradients around dissolving crystals (e.g., Zhang et al., 1989). Mean boundary layer compositions will therefore lie between those of dissolving crystals and their host melts. This may account for the slightly lower  $\text{Mg}\#$  of most clinopyroxene inclusion and nodule clinopyroxene rim analyses (i.e., those not associated with pockets of late-stage crystallization) with respect to nodule clinopyroxene core analyses (Figure 5). Boundary layer compositions will also depend on the relative diffusivities of different elements, meaning that some exchange with the surrounding melt is highly likely to occur; even convectively stable boundary layers are unlikely to be fully isolated from the surrounding melt. Complex multicomponent effects notwithstanding (e.g., Liang et al., 1996), Na typically diffuses more quickly than other major species in silicate melts (Zhang et al., 2010b), providing a mechanism by which initially Na-poor boundary layers could have acquired sufficient Na to crystallize  $X_{\text{An}} \leq 0.82$  plagioclase. In contrast, Al diffuses more slowly than most other major species in silicate melts (Chen and Zhang, 2008; Yu et al., 2016), providing a mechanism by which Al-poor boundary layers formed by dissolution could have

been preserved during magma ascent (cf. Neave et al., 2017b). However, evaluating the exact composition of boundary layers in sample JM27 would be challenging, and we suggest that such information would be best recovered from glassy nodules with feasibly intact boundary layers (e.g., Gurenko and Sobolev, 2006).

The narrowest nodule clinopyroxene rims we observed are typically 50–100  $\mu\text{m}$  wide (Figures 3A,B). These minimum rim widths provide our best estimates of the distances that nodule clinopyroxene cores dissolved during ascent. This is because they are probably associated with crystal faces oriented normal to the plane of the thin section that are hence minimally affected by 3-D cutting effects (e.g., Shea et al., 2015). Moreover, rim widths do not appear to vary substantially between different crystal faces, indicating that mineral anisotropy does not significantly affect clinopyroxene dissolution lengthscales in sample JM27. Clinopyroxene inclusions and embayments probably resulted from dissolution over greater distances than 100  $\mu\text{m}$ , but may also reflect the exploitation of pre-existing fractures and cleavage planes (Chen and Zhang, 2009). It is also possible that the development of dissolution channels in 3-D may have affected the apparent dissolution lengths visible in 2-D. Importantly, the geometry of the wehrlitic nodule investigated here means that nodule clinopyroxene rims were largely protected from turbulence in the external magma during ascent. That is, we expect that nodule clinopyroxene rims record dissolution that was primarily diffusive rather than convective in nature (Kerr, 1995; Zhang and Xu, 2003). As a consequence, the thickness of nodule clinopyroxene rims encodes robust information about clinopyroxene dissolution times that can be used to estimate magma decompression and ascent rates.

## 6. MODELING CLINOPYROXENE DISSOLUTION

Experimental investigations of clinopyroxene dissolution by Chen and Zhang (2009) provide a framework for modeling clinopyroxene dissolution recorded in the Borgarhraun lava flow. Specifically, Chen and Zhang (2009) characterized rates of diffusive diopside dissolution into a tholeiitic basalt by experimentally dissolving diopside crystals at a range of pressures and temperatures. They then used their experimental results to calibrate a model from which dissolution time could be predicted as a function of pressure, temperature, melt composition, clinopyroxene composition and dissolution length. We do however note the important limitation that Chen and Zhang (2009) did not incorporate any effects of mineral anisotropy into their simplified model. Nevertheless, coherence in their experimental results suggests that anisotropy exerts only second order effects over crystal dissolution rates. Importantly, dissolution experiments were carefully designed to avoid convection, making the resulting model well-suited for estimating dissolution times from the nodule clinopyroxene rims we describe here. Furthermore, the high- $\text{Mg}\#_{\text{cpx}}$  compositions from the Borgarhraun lava flow are amongst the closest to pure diopside of any known compositions from Iceland (MacLennan et al., 2003a; Winpenny and MacLennan, 2011), making the

Borgarhraun eruption an ideal candidate for estimating magma decompression and ascent rates using a model based on diopside dissolution. Moreover, clinopyroxene crystals in JM27 are free from exsolution lamellae that may complicate the interpretation of features created by diffusion and dissolution processes (e.g., Dohmen and Milke, 2010).

Chen and Zhang (2009) provided a series of five equations (their Equations 4, 5a–5d) that, in theory, can be solved iteratively to obtain the parameters required to quantitatively relate dissolution length and dissolution time in diopside-liquid systems. However, our attempts to iteratively solve these equations with the `optim()` function in the `stats` package of R often failed to converge (R Development Core Team, 2016), making it difficult to explore clinopyroxene stability across diverse pressure and temperature conditions. We therefore rearranged the equations of Chen and Zhang (2009) to reduce the number of unknown parameters from five to one, allowing the single remaining unknown parameter (the fitting parameter  $\alpha$ ) to be obtained through a more stable root-finding approach implemented with the `uniroot()` function in the `stats` package of R. These rearrangements are documented below.

As described by Chen and Zhang (2009) in their Equation (2a), chemical profiles in melts adjacent to dissolving crystals can be described by the 1-D diffusive dissolution equation (Crank, 1975):

$$C = C_\infty + (C_0 - C_\infty) \frac{\operatorname{erfc}\left(\frac{x}{2\sqrt{Dt}} - \alpha\right)}{\operatorname{erfc}(-\alpha)}, \quad (1)$$

where  $C$  is the concentration of a component in the melt,  $C_0$  is concentration in the melt at the crystal-melt interface and  $C_\infty$  is the far-field concentration.  $x$  is the distance from the crystal-melt interface,  $D$  is the effective binary diffusivity of the element or oxide in question and  $t$  is duration of experiment.  $\alpha$  is a fitting parameter related to the dissolution rate that, as per Equation (2b) of Chen and Zhang (2009), satisfies:

$$\exp(\alpha^2) \operatorname{erfc}(-\alpha) \sqrt{\pi} \alpha = \frac{C_0 - C_\infty}{C_c - C_0}, \quad (2)$$

where  $C_c$  is the concentration of the element or oxide in question in the crystal.

As per Equation (2c) of Chen and Zhang (2009), the crystal diffusive dissolution distance can be expressed as:

$$L = 2\alpha \frac{\rho_m}{\rho_c} \sqrt{Dt}, \quad (3)$$

where  $\rho_m$  and  $\rho_c$  are the densities of melt and crystal, respectively.

The stability of clinopyroxene crystals in basaltic melts is mediated, in part, by the diffusion of Mg and Ca cations within their host liquids (Chen and Zhang, 2009); the diffusion of Mg and Ca within clinopyroxene crystals is many orders of magnitude slower than within basaltic melts (Zhang et al., 2010a), and thus does not affect clinopyroxene stability over the timescales of interest here. As per Equations (3a) and (3b) of

Chen and Zhang (2009), Mg and Ca diffusion within basaltic melts can be described by:

$$\ln D_{\text{Mg}} = -6.664(\pm 0.745) - \frac{28897 \pm 1221(2\sigma)}{T}, \quad (4)$$

and:

$$\ln D_{\text{Ca}} = -10.517(\pm 0.901) - \frac{21205 \pm 1476(2\sigma)}{T}, \quad (5)$$

where  $T$  is in K and  $D$  is in  $\text{m}^2 \cdot \text{s}^{-1}$ .

As per Equation (4) of Chen and Zhang (2009), the saturation condition at the clinopyroxene-melt interface can be expressed when:

$$\ln(C_0^{\text{Mg}} \times C_0^{\text{Ca}}) = a + bP + \frac{e}{T} + g \frac{P^2}{T^2}, \quad (6)$$

where  $C_0$  values are expressed in oxide wt.%,  $P$  is pressure in GPa and  $a$ ,  $b$ ,  $e$  and  $g$  are fitting parameters with values of  $22.85 \pm 1.82(2\sigma)$ ,  $2.10 \pm 0.44(2\sigma)$ ,  $26360 \pm 2565(2\sigma)$ , and  $1.22 \pm 0.43(2\sigma) \times 10^6$ , respectively.

Rearranging Equation (6) and gathering the terms then allows us to define a function in which  $C_0^{\text{Mg}} \times C_0^{\text{Ca}}$  depends upon  $P$  and  $T$  alone:

$$H(P, T) = a + bP + \frac{e}{T} + g \frac{P^2}{T^2}, \quad (7)$$

and thus:

$$C_0^{\text{Mg}} \times C_0^{\text{Ca}} = \exp(H(P, T)) = h(P, T). \quad (8)$$

Given that  $L$  is equal for both MgO and CaO, Equation (3) leads to the expression:

$$\alpha_{\text{Mg}} = \alpha_{\text{Ca}} \sqrt{\frac{D_{\text{Ca}}}{D_{\text{Mg}}}}. \quad (9)$$

If we define:

$$f(\alpha) = \exp(\alpha^2) \operatorname{erfc}(-\alpha) \sqrt{\pi} \alpha, \quad (10)$$

then rearranging Equation (2) provides:

$$f(\alpha) = \frac{C_0 - C_\infty}{C_c - C_0}. \quad (11)$$

Given that, as per Equation (8),  $C_0^{\text{Mg}} = h/C_0^{\text{Ca}}$ , then:

$$f(\alpha_{\text{Mg}}) = \frac{(h/C_0^{\text{Ca}}) - C_\infty^{\text{Mg}}}{C_c^{\text{Mg}} - (h/C_0^{\text{Ca}})}, \quad (12)$$

and:

$$f(\alpha_{Ca}) = \frac{C_0^{Ca} - C_\infty^{Ca}}{C_c^{Ca} - C_0^{Ca}} \quad (13)$$

Rearranging these equations then gives:

$$C_0^{Ca} = \frac{h[1 + f(\alpha_{Mg})]}{f(\alpha_{Mg})C_c^{Mg} + C_\infty^{Mg}} = \frac{f(\alpha_{Ca})C_c^{Ca} + C_\infty^{Ca}}{1 + f(\alpha_{Ca})} \quad (14)$$

and therefore:

$$h[1 + f(\alpha_{Mg})][1 + f(\alpha_{Ca})] = [f(\alpha_{Ca})C_c^{Ca} + C_\infty^{Ca}] [f(\alpha_{Mg})C_c^{Mg} + C_\infty^{Mg}] \quad (15)$$

A root finding approach can then be used to find values of  $\alpha_{Mg}$  where the following expression is zero and substitutions are made using Equation (9):

$$Q = h[1 + f(\alpha_{Mg})][1 + f(\alpha_{Ca})] - [f(\alpha_{Ca})C_c^{Ca} + C_\infty^{Ca}] [f(\alpha_{Mg})C_c^{Mg} + C_\infty^{Mg}] \quad (16)$$

and Equation (3) can then be used to calculate  $t$ .

The results of dissolution calculations performed assuming a fixed dissolution time of 1 s are presented in **Figure 7** and demonstrate the strong effects of pressure and temperature on the stability of clinopyroxene with the mean composition of nodule clinopyroxene cores in the Borgarhraun matrix glass composition reported by Sigurdsson et al. (2000). Calculated clinopyroxene liquidus temperatures vary from  $\sim 1,190^\circ\text{C}$  at 1 atm to  $\sim 1,320^\circ\text{C}$  at 800 MPa and are encouragingly consistent with the results of calculations with the MELTS algorithm (**Figure 1**). These calculations also illustrate the strong dependence of dissolution rate on temperature and hence the vital importance of estimating magma eruption temperatures accurately when determining magma decompression and ascent rates from clinopyroxene dissolution lengths.

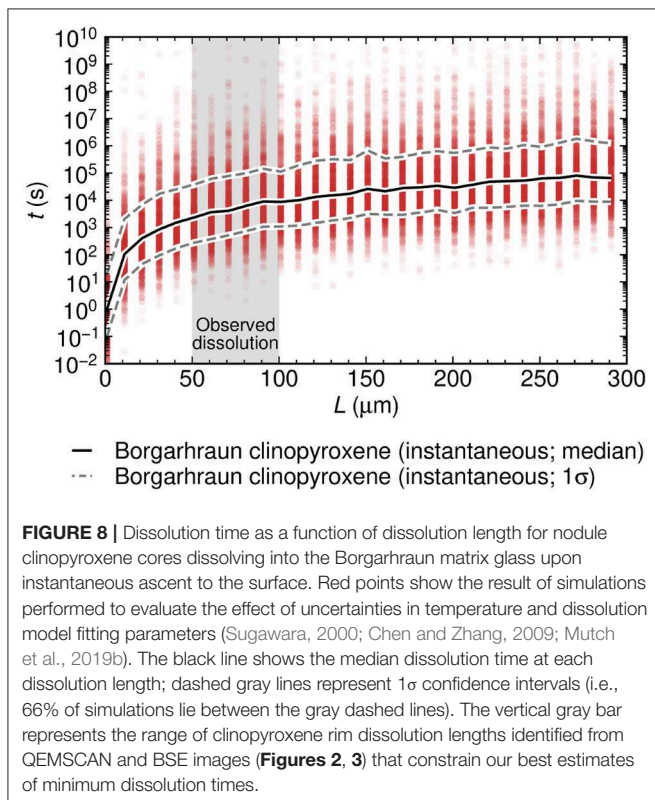
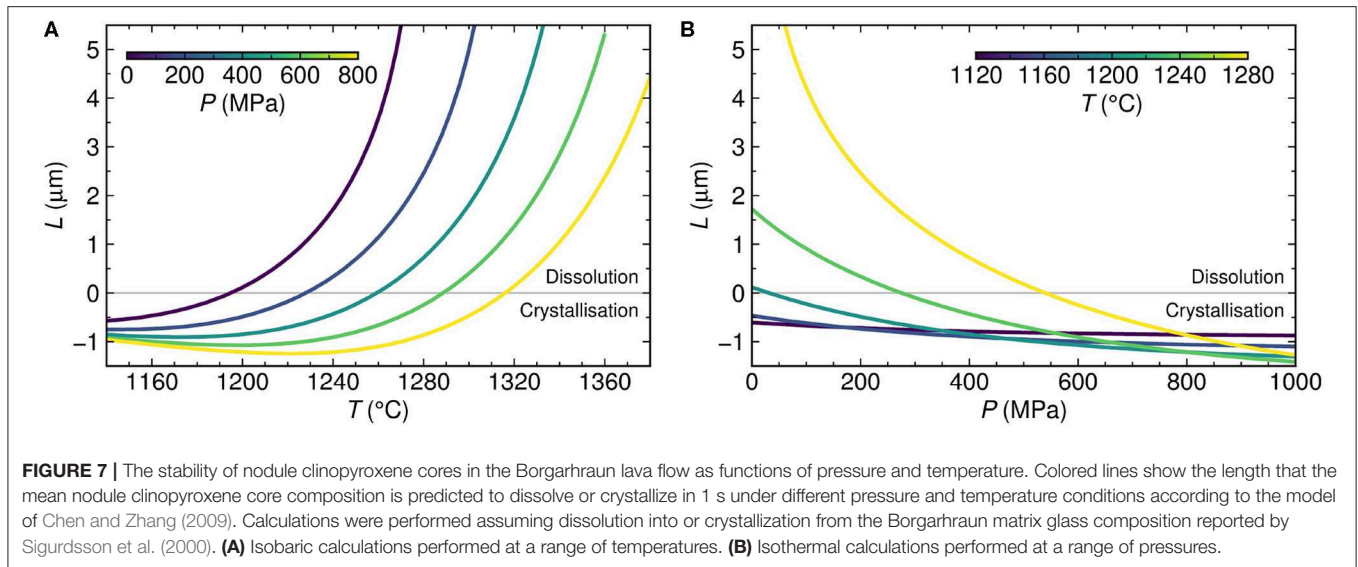
Indicative clinopyroxene dissolution times for the Borgarhraun lava flow were estimated by assuming that all dissolution took place at the surface following instantaneous magma ascent from near-Moho depths (**Figure 8**). A magma temperature of  $1,230^\circ\text{C}$  was taken from Mutch et al. (2019b) who performed calculations with the geothermometer of Sugawara (2000) that has an associated model SEE of  $30^\circ\text{C}$ . The temperature decrease associated with adiabatic cooling of the ascending magma over the pressure interval of relevance is well within the SEE of the geothermometer used ( $<8^\circ\text{C}$  over 215 MPa; see below; Katz et al., 2003), and is thus not considered further. Uncertainties in dissolution time estimates were evaluated by resampling ( $n = 1,000$ ) temperature and fitting parameters in Equation (6) for each dissolution length increment according to their respective uncertainties (Sugawara, 2000; Chen and Zhang, 2009). Resulting median dissolution

times range from 30 min for a dissolution length of  $50 \mu\text{m}$  to 150 min for a dissolution length of  $100 \mu\text{m}$ —the range of minimum observed dissolution lengths (**Figure 3**). Lower  $1\sigma$  bounds on dissolution times (i.e., 17th percentiles) are typically a factor of ten shorter than the median times and  $1\sigma$  bounds (83rd percentiles) are typically a factor of 18 longer. Dissolution times are thus associated with  $1\sigma$  uncertainties on the order of one order of magnitude which primarily reflect uncertainties in magma eruption temperatures that are challenging to overcome with currently available approaches (Putirka, 2008).

Mean magma decompression rates were estimated from clinopyroxene dissolution times by assuming that dissolution started as soon the ascending magma reached a pressure of 215 MPa, the pressure at which Equations (3) and (6) predict a change from clinopyroxene crystallization to clinopyroxene dissolution (**Figure 7**). Estimated mean decompression rates vary from  $110 \text{ kPa}\cdot\text{s}^{-1}$  for a dissolution length of  $50 \mu\text{m}$  to  $24 \text{ kPa}\cdot\text{s}^{-1}$  for a dissolution length of  $100 \mu\text{m}$  (**Figure 9A**). Estimated rates increase substantially to  $210 \text{ MPa}\cdot\text{s}^{-1}$  for a dissolution length of  $5 \mu\text{m}$ , and decrease modestly to  $3.3 \text{ kPa}\cdot\text{s}^{-1}$  for a dissolution length of  $300 \mu\text{m}$ . Mean magma ascent rates were estimated by converting the clinopyroxene saturation pressure of 215 MPa into a depth of 7.6 km by assuming a mean crustal density of  $2.88 \text{ Mg}\cdot\text{m}^{-3}$  (MacLennan et al., 2001). Resulting mean ascent rate estimates vary from  $3.9 \text{ m}\cdot\text{s}^{-1}$  for a dissolution length of  $50 \mu\text{m}$  to  $0.85 \text{ m}\cdot\text{s}^{-1}$  for a dissolution length of  $100 \mu\text{m}$  (**Figure 9B**), and are subject to propagated uncertainties on order of one order of magnitude. However, assuming that all dissolution occurred at the surface following instantaneous ascent is likely to overestimate true magma decompression and ascent rates because it unrealistically implies that all dissolution occurred under the highest possible degrees of disequilibrium. In line with other studies (e.g., Lloyd et al., 2014; Mutch et al., 2019b; Newcombe et al., 2020), we therefore performed additional calculations with the more naturalistic assumption that magma ascended at a constant rate.

Assuming that clinopyroxene dissolution took place in response to decompression at a constant rate, dissolution lengths of  $50$  and  $100 \mu\text{m}$  imply decompression rates of  $15$  and  $3.0 \text{ kPa}\cdot\text{s}^{-1}$  respectively (**Figure 9A**). These values are approximately one order of magnitude lower than the mean decompression rates estimated by assuming that all dissolution took place following instantaneous ascent. Estimated magma ascent rates are also correspondingly lower:  $0.53$  and  $0.11 \text{ m}\cdot\text{s}^{-1}$  for dissolution lengths of  $50$  and  $100 \mu\text{m}$  respectively (**Figure 9B**). The difference between rates estimated with instantaneous and constant-rate assumptions primarily reflects the dependence of clinopyroxene dissolution rate on pressure (**Figure 7**). That is, clinopyroxene dissolution rates are much lower at high pressures where disequilibrium is negligible than at the surface where disequilibrium is greatest, meaning that very little clinopyroxene dissolves during the initial stages of clinopyroxene-undersaturated magma decompression.

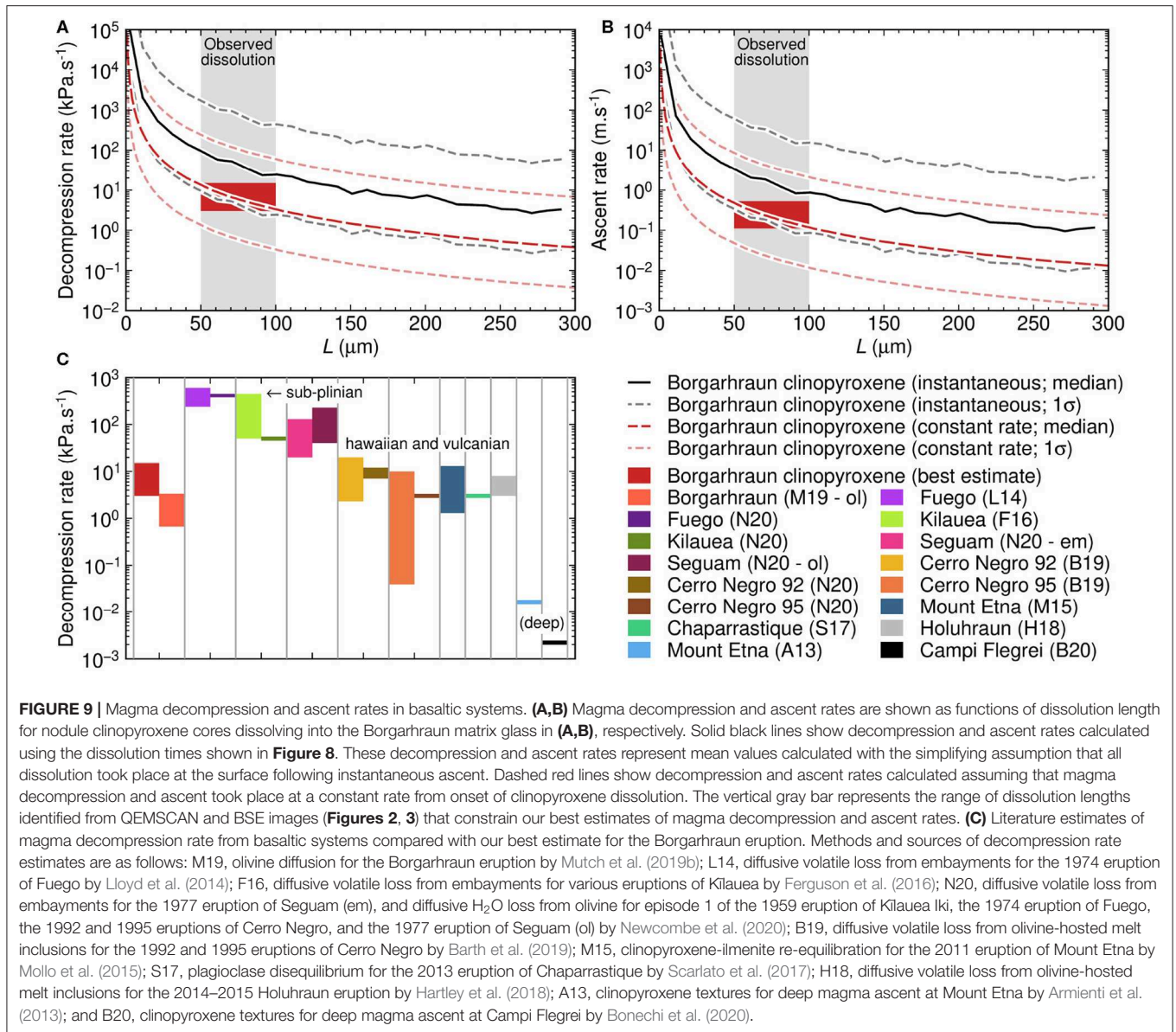
Magma decompression rates estimated from clinopyroxene dissolution are compared with those estimated from the diffusive re-equilibration of primitive olivine crystals carried by the Borgarhraun magma in **Figure 9C** (Mutch et al., 2019b).



Encouragingly, our best estimates ( $3.0\text{--}15\text{ kPa}\cdot\text{s}^{-1}$ ) are broadly comparable with those obtained from a wholly independent diffusion chronometry approach for the same eruption ( $0.7\text{--}3.3\text{ kPa}\cdot\text{s}^{-1}$ ). Our findings thus corroborate those of Mutch et al. (2019b) who estimated a mean magma ascent rate of  $0.02\text{--}0.1\text{ m}\cdot\text{s}^{-1}$ , and confirm that transcrustal magma transport in Iceland may be considerably more rapid than reported in arc

settings ( $0.5\text{--}1\text{ mm}\cdot\text{s}^{-1}$ ; Ruprecht and Plank, 2013). On the basis of comparisons with transcrustal transport estimates from Mutch et al. (2019b), our best estimates also suggest that the Borgarhraun magma ascended more rapidly near the surface than it did at depth, consistent with either the upward acceleration of rising magma or the convolution of isobaric intervals of magma mixing with polybaric intervals of magma ascent by diffusion-based methods.

Magma decompression rates estimated for the Borgarhraun eruption are compared with published estimates from other basaltic systems in Figure 9C. Note that we compare decompression rather than ascent rates in order to avoid introducing additional uncertainties from converting pressures to depths across a range of different settings with different crustal density structures. Perhaps unsurprisingly, our best decompression rate estimates for the Borgarhraun eruption ( $3.0\text{--}15\text{ kPa}\cdot\text{s}^{-1}$ ) are about two orders of magnitude lower than those reported for the sub-plinian 1974 eruption of Volcán de Fuego, Guatemala, based on the loss of volatiles from melt embayments and the loss of  $\text{H}_2\text{O}$  from olivine crystals ( $240\text{--}600$  and  $380\text{--}450\text{ kPa}\cdot\text{s}^{-1}$ , respectively; Lloyd et al., 2014; Newcombe et al., 2020). Decompression rates estimated from the loss of volatiles from melt embayments for a series of Hawaiian to sub-plinian eruptions of Kilauea, Hawaii, are also greater than those estimated for the Borgarhraun eruption ( $50\text{--}450\text{ kPa}\cdot\text{s}^{-1}$ ), with the greatest Kilauean rates being associated with the most explosive, sub-plinian eruptions (Ferguson et al., 2016). Indeed, decompression rates estimated for episode 1 of the Hawaiian 1959 Kilauea Iki eruption from both the loss of volatiles from melt embayments and the loss of  $\text{H}_2\text{O}$  from olivine crystals are only about one order of magnitude greater than our estimates for the Borgarhraun eruption ( $\sim 50\text{ kPa}\cdot\text{s}^{-1}$ ; Ferguson et al., 2016; Newcombe et al., 2020). Similar rates also been estimated for the Hawaiian 1977 eruption of Seguam, Alaska, using the same techniques ( $20\text{--}130\text{ kPa}\cdot\text{s}^{-1}$  from embayments and  $40\text{--}230\text{ kPa}\cdot\text{s}^{-1}$  from olivine; Newcombe et al., 2020). Thus, magmas



that have fed explosive basaltic eruptions ranging from Hawaiian to sub-plinian in style have typically decompressed more rapidly than the magma that fed the Borgarhraun eruption. However, this does not appear to have been the case for all explosively erupted basaltic magmas.

Decompression rates estimated for two moderately explosive eruptions of Cerro Negro, Nicaragua, in 1992 (VEI3, likely vulcanian) and 1995 (VEI2, likely Hawaiian) are broadly similar to those estimated for the Borgarhraun eruption, especially in the case of less explosive 1995 eruption (Barth et al., 2019; Newcombe et al., 2020). Specifically, rates estimated for the 1992 and 1995 eruptions from the loss of volatiles from melt embayments are 2.3–20 and 0.039–10 kPa.s<sup>-1</sup> respectively (Barth et al., 2019), and those from the loss of H<sub>2</sub>O from olivine crystals are 7–12 and 3 kPa.s<sup>-1</sup> respectively (Newcombe et al., 2020). Decompression rates comparable to those from

the Borgarhraun eruption have also been reported for the vulcanian 2013 eruption of Chaparrastique, El Salvador, based on plagioclase dissolution textures (~3 kPa.s<sup>-1</sup>; Scarlato et al., 2017). Although deep magma decompression rates of ~16 and ~2.2 Pa.s<sup>-1</sup> beneath Mount Etna and Campi Flegrei, Italy, estimated from clinopyroxene textures by Armienti et al. (2013) and Bonechi et al. (2020) respectively are about three orders of magnitude lower than our best estimates for the Borgarhraun eruption, shallow decompression rates estimated for Hawaiian eruptions of Mount Etna in 2011 on the basis of clinopyroxene-ilmenite re-equilibration are very similar to those we report here (1.3–13 kPa.s<sup>-1</sup>; Mollo et al., 2015). Finally, we note that our estimated decompression rates overlap with those obtained by modeling the diffusive loss of H<sub>2</sub>O from moderately evolved olivine-hosted melt inclusions in magmatic tephra collected during weakly Hawaiian phases of the 2014–2015 Holuhraun

eruption, Iceland ( $3\text{--}8\text{ kPa}\cdot\text{s}^{-1}$ ; Hartley et al., 2018). During its final ascent, the Borgarhraun magma therefore appears to have decompressed as rapidly as magmas that have fed various explosive basaltic eruptions ranging from Hawaiian to vulcanian in style.

The magma decompression rates that both we and Mutch et al. (2019b) estimate for the dominantly effusive and at most transiently explosive Borgarhraun eruption are broadly consistent with recently established relationships between explosivity and magma decompression rate (e.g., Barth et al., 2019). Namely, we find that the effusively erupted Borgarhraun magma decompressed more slowly than the magmas that fed basaltic sub-plinian eruptions at Fuego and Kilauea. However, differences in magma decompression rate are modest or even absent when comparing the Borgarhraun eruption with Hawaiian and vulcanian eruptions at Cerro Negro, Chaparrastique and Mount Etna. Our calculations thus suggest that effusively erupted  $\text{H}_2\text{O}$ -poor basalts from ocean island and mid-ocean ridge settings can decompress and ascend through the shallow crust just as rapidly as some explosively erupted  $\text{H}_2\text{O}$ -rich basalts from arc settings. Moreover, it seems unlikely that the ascent rates of basaltic magmas are simply related to their  $\text{H}_2\text{O}$  contents. Although  $\text{H}_2\text{O}$  exsolution certainly plays a major role in driving the ascent of myriad magma types, other factors, such as melt buoyancy and  $\text{CO}_2$  exsolution must therefore drive the rapid ascent of primitive and  $\text{H}_2\text{O}$ -poor basalts like the Borgarhraun magma.

Comparing rates of shallow, syn-eruptive magma decompression (including our estimate for the Borgarhraun eruption) with those for deep decompression associated with inter-eruptive magma assembly beneath Mount Etna and Campi Flegrei (Figure 9C; Armienti et al., 2013; Bonechi et al., 2020), suggests that magmas ascend much more rapidly during eruptions than during pre-eruptive magma recharge at depth. Magma transport leading to eruption may therefore operate in a fundamentally different way from magma transport out of the mantle and between magma reservoirs. It thus remains unclear how well seismic signals of inter-eruptive magma transport reflect likely rates of pre-eruptive magma ascent (White et al., 2011; Tarasewicz et al., 2012; Mutch et al., 2019b). Indeed, our results suggest that primitive and  $\text{H}_2\text{O}$ -poor basalts may erupt with no more than a few days' precursory warning, making it challenging to evaluate the risks posed by some basaltic volcanoes.

## 7. CONCLUSIONS

Mineral textures and compositions in a wehrlitic nodule from the primitive Borgarhraun lava flow erupted in North Iceland record clinopyroxene dissolution during magma ascent from near-Moho depths. Mapping the distribution of Al distinguishes high- $\text{Al}_2\text{O}_3$  clinopyroxene cores from low- $\text{Al}_2\text{O}_3$  clinopyroxene rims and inclusions. The high  $\text{Al}_2\text{O}_3$  content of clinopyroxene cores is consistent with crystallization at  $\sim 800\text{ MPa}$ , in line with published estimates of pre-eruptive magma storage pressures. In contrast, the low  $\text{Al}_2\text{O}_3$  of clinopyroxene rims and inclusions is

consistent with crystallization at or near the surface. Given that clinopyroxene rim and inclusion boundaries cut across sector zone boundaries within resorbed clinopyroxene cores, we infer that high- $\text{Al}_2\text{O}_3$  clinopyroxene cores dissolved during ascent as a consequence of the strong dependence of clinopyroxene stability on pressure. We thus interpret clinopyroxene rims and inclusions as recrystallized boundary layers protected from convective or turbulent dissipation by their host nodule. Corroborating evidence for clinopyroxene dissolution is provided by plagioclase and titanomagnetite crystals within clinopyroxene rims and inclusions that occur in proportions consistent with low-pressure crystallization of molten high- $\text{Al}_2\text{O}_3$  clinopyroxene cores during lava flow emplacement. Our findings are supported by textural and geochemical observations from across Iceland that indicate a potentially widespread role for clinopyroxene dissolution in basalt petrogenesis. It thus seems feasible that clinopyroxene dissolution could occur within any vertically extensive basaltic plumbing system and could hence offer a compelling explanation for the pyroxene paradox reported from mid-ocean ridge basalts.

Experimental calibrations of clinopyroxene stability suggest clinopyroxene began to dissolve once the Borgarhraun magma decompressed below the pressure of clinopyroxene saturation at  $215\text{ MPa}$ . Our best decompression rate estimates of  $3.0\text{--}15\text{ kPa}\cdot\text{s}^{-1}$  were obtained from calculations assuming that decompression took place at a constant rate. These estimates could nonetheless be improved in future by quantifying the effects of mineral anisotropy on clinopyroxene dissolution kinetics with further experiments. Converting magma decompression rates into magma ascent rates results in values of  $0.11\text{--}0.53\text{ m}\cdot\text{s}^{-1}$  that are similar published estimates obtained from the diffusive re-equilibration of olivine (Mutch et al., 2019b). Nevertheless, our ascent rates are slightly faster than these published values, consistent with magma acceleration during ascent or the temporary stalling of magma after mush disaggregation. Although the Borgarhraun eruption broadly conforms to global correlations between eruption explosivities and magma decompression rates, the decompression rates we estimate are comparable to those obtained from some moderately explosive basaltic eruptions in arc settings, implying that there is no simple relationship between magma decompression rate and magma  $\text{H}_2\text{O}$  content. Indeed, comparing magma ascent rates from Iceland with those from arc settings suggests that primitive and  $\text{H}_2\text{O}$ -poor basalts can traverse the crust considerably faster than some  $\text{H}_2\text{O}$ -rich basalts, though further work is required to evaluate how ascent rates are affected by the differing structures of mid-ocean ridge, ocean island and arc plumbing systems. It is, however, clear that magmas tapped from reservoirs near the Moho in ocean island and mid-ocean ridge settings may reach the surface within days. This represents a major challenge when evaluating the risks posed by infrequent but nonetheless potentially hazardous eruptions of primitive basalt.

## DATA AVAILABILITY STATEMENT

All datasets generated for this study are included in the article/Supplementary Material.

## AUTHOR CONTRIBUTIONS

DN and JM co-designed the project. DN performed the BSE imaging and EPMA, implemented the clinopyroxene dissolution model, and wrote the manuscript. JM collected the sample, facilitated the QEMSCAN imaging, rearranged the equations of Chen and Zhang (2009), and contributed to writing the manuscript.

## FUNDING

DN and this work were supported by a Presidential Fellowship from the University of Manchester.

## ACKNOWLEDGMENTS

We thank Lewis Hughes for assisting with BSE imaging at the University of Manchester and Iris Buisman for performing QEMSCAN imaging and assisting with EPMA at the University

of Cambridge. We also thank CP and SM for their insightful and constructive reviews, and MP for his efficient editorial handling.

## SUPPLEMENTARY MATERIAL

The Supplementary Material for this article can be found online at: <https://www.frontiersin.org/articles/10.3389/feart.2020.00188/full#supplementary-material>

**Supplementary Data Sheet 1** | Raw BSE images.

**Supplementary Table 1** | EMPA data.

**Supplementary Figure 1** | JM21 4  $\mu\text{m}$  QEMSCAN AI Map.

**Supplementary Figure 2** | JM21 4  $\mu\text{m}$  QEMSCAN Phase Map.

**Supplementary Figure 3** | JM24 4  $\mu\text{m}$  QEMSCAN AI Map.

**Supplementary Figure 4** | JM24 4  $\mu\text{m}$  QEMSCAN Phase Map.

**Supplementary Figure 5** | JM27 4  $\mu\text{m}$  QEMSCAN AI Map.

**Supplementary Figure 6** | JM27 4  $\mu\text{m}$  QEMSCAN Phase Map.

**Supplementary Figure 7** | QEMSCAN legend.

## REFERENCES

- Aoki, K., and Kushiro, I. (1968). Some clinopyroxenes from ultramafic inclusions in Dreiser Weiher, Eifel. *Contrib. Mineral. Petrol.* 18, 326–337. doi: 10.1007/BF00399694
- Armienti, P., Perinelli, C., and Putirka, K. D. (2013). A new model to estimate deep-level magma ascent rates, with applications to Mt. Etna (Sicily, Italy). *J. Petrol.* 54, 795–813. doi: 10.1093/petrology/egs085
- Barth, A., Newcombe, M., Plank, T., Gonnermann, H., Hajimirza, S., Soto, G. J., et al. (2019). Magma decompression rate correlates with explosivity at basaltic volcanoes—constraints from water diffusion in olivine. *J. Volcanol. Geotherm. Res.* 387:106664. doi: 10.1016/j.jvolgeores.2019.106664
- Bender, J. F., Hodges, F. N., and Bence, A. E. (1978). Petrogenesis of basalts from the project FAMOUS area: experimental study from 0 to 15 kbars. *Earth Planet. Sci. Lett.* 41, 277–302. doi: 10.1016/0012-821X(78)90184-X
- Blundy, J. D., Falloon, T. J., Wood, B. J., and Dalton, J. A. (1995). Sodium partitioning between clinopyroxene and silicate melts. *J. Geophys. Res. Solid Earth* 100, 15501–15515. doi: 10.1029/95JB00954
- Bonechi, B., Perinelli, C., and Gaeta, M. (2020). Clinopyroxene growth rates at high pressure: constraints on magma recharge of the deep reservoir of the Campi Flegrei Volcanic District (south Italy). *Bull. Volcanol.* 82:5. doi: 10.1007/s00445-019-1342-5
- Brearley, M., and Scarfe, C. M. (1986). Dissolution rates of upper mantle minerals in an alkali basalt melt at high pressure: an experimental study and implications for ultramafic xenolith survival. *J. Petrol.* 27, 1157–1182. doi: 10.1093/petrology/27.5.1157
- Cashman, K. V., Sparks, R. S. J., and Blundy, J. D. (2017). Vertically extensive and unstable magmatic systems: a unified view of igneous processes. *Science* 355:eaag3055. doi: 10.1126/science.aag3055
- Cassidy, M., Manga, M., Cashman, K. V., and Bachmann, O. (2018). Controls on explosive-effusive volcanic eruption styles. *Nat. Commun.* 9:2839. doi: 10.1038/s41467-018-05293-3
- Chen, Y., and Zhang, Y. (2008). Olivine dissolution in basaltic melt. *Geochim. Cosmochim. Acta* 72, 4756–4777. doi: 10.1016/j.gca.2008.07.014
- Chen, Y., and Zhang, Y. (2009). Clinopyroxene dissolution in basaltic melt. *Geochim. Cosmochim. Acta* 73, 5730–5747. doi: 10.1016/j.gca.2009.06.016
- Cooper, G. F., Davidson, J. P., and Blundy, J. D. (2016). Plutonic xenoliths from Martinique, Lesser Antilles: evidence for open system processes and reactive melt flow in island arc crust. *Contrib. Mineral. Petrol.* 171:87. doi: 10.1007/s00410-016-1299-8
- Crank, J. (1975). *The Mathematics of Diffusion. 2nd Edn.* Oxford: Clarendon Press.
- Dohmen, R., and Milke, R. (2010). Diffusion in polycrystalline materials: grain boundaries, mathematical models, and experimental data. *Rev. Mineral. Geochem.* 72, 921–970. doi: 10.2138/rmg.2010.72.21
- Eason, D. E., and Sinton, J. M. (2009). Lava shields and fissure eruptions of the Western Volcanic Zone, Iceland: evidence for magma chambers and crustal interaction. *J. Volcanol. Geotherm. Res.* 186, 331–348. doi: 10.1016/j.jvolgeores.2009.06.009
- Ferguson, D. J., Gonnermann, H. M., Ruprecht, P., Plank, T. A., Hauri, E. H., Houghton, B. F., et al. (2016). Magma decompression rates during explosive eruptions of Kilauea volcano, Hawaii, recorded by melt embayments. *Bull. Volcanol.* 78:71. doi: 10.1007/s00445-016-1064-x
- Freer, R., Carpenter, M. A., Long, J. V. P., and Reed, S. J. B. (1982). “Null result” diffusion experiments with diopside: implications for pyroxene equilibria. *Earth Planet. Sci. Lett.* 58, 285–292. doi: 10.1016/0012-821X(82)90201-1
- Fujii, T., and Bougault, H. (1983). Melting relations of a magnesian abyssal tholeiite and the origin of MORBs. *Earth Planet. Sci. Lett.* 62, 283–295. doi: 10.1016/0012-821X(83)90091-2
- Ghiorso, M. S., and Sack, R. O. (1995). Chemical mass transfer in magmatic processes IV. A revised and internally consistent thermodynamic model for the interpolation and extrapolation of liquid-solid equilibria in magmatic systems at elevated temperatures and pressures. *Contrib. Mineral. Petrol.* 119, 197–212. doi: 10.1007/s004100050036
- Gonnermann, H. M., and Manga, M. (2007). The fluid mechanics inside a volcano. *Annu. Rev. Fluid Mech.* 39, 321–356. doi: 10.1146/annurev.fluid.39.050905.110207
- Grove, T. L., Kinzler, R. J., and Bryan, W. B. (1992). “Fractionation of mid-ocean ridge basalt (MORB),” in *Mantle Flow and Melt Generation at Mid-Ocean Ridges, Geophysical Monograph, Vol. 71*, eds J. P. Morgan, D. K. Blackman, and J. M. Sinton (Washington DC: American Geophysical Union), 281–310. doi: 10.1029/GM071p0281
- Gurenko, A. A., and Sobolev, A. V. (2006). Crust-primitive magma interaction beneath neovolcanic rift zone of Iceland recorded in gabbro xenoliths from Midfell, SW Iceland. *Contrib. Mineral. Petrol.* 151, 495–520. doi: 10.1007/s00410-006-0079-2
- Halldórsson, S. A., Óskarsson, N., Grönvold, K., Sigurdsson, G., Sverrisdóttir, G., and Steinthórsson, S. (2008). Isotopic-heterogeneity of the Thjorsa lava-Implications for mantle sources and crustal processes within the Eastern Rift Zone, Iceland. *Chem. Geol.* 255, 305–316. doi: 10.1016/j.chemgeo.2008.06.050
- Hansen, H., and Grönvold, K. (2000). Plagioclase ultraphyric basalts in Iceland: the mush of the rift. *J. Volcanol. Geotherm. Res.* 98, 1–32. doi: 10.1016/S0377-0273(99)00189-4



- Hansteen, T. H. (1991). Multi-stage evolution of the picritic Mælifell rocks, SW Iceland: constraints from mineralogy and inclusions of glass and fluid in olivine. *Contrib. Mineral. Petrol.* 109, 225–239. doi: 10.1007/BF00306481
- Hartley, M. E., Bali, E., MacLennan, J., Neave, D. A., and Halldórsson, S. A. (2018). Melt inclusion constraints on petrogenesis of the 2014–2015 Holuhraun eruption, Iceland. *Contrib. Mineral. Petrol.* 173:10. doi: 10.1007/s00410-017-1435-0
- Holland, T. J. B., Green, E. C. R., and Powell, R. (2018). Melting of peridotites through to granites: a simple thermodynamic model in the system KNCFMASHTOCr. *J. Petrol.* 59, 881–900. doi: 10.1093/petrology/egy048
- Holness, M. B., Anderson, A. T., Martin, V. M., MacLennan, J., Passmore, E., and Schwindinger, K. R. (2007). Textures in partially solidified crystalline nodules: a window into the pore structure of slowly cooled mafic intrusions. *J. Petrol.* 48, 1243–1264. doi: 10.1093/petrology/egm016
- Holness, M. B., Stripp, G., Humphreys, M. C. S., Veksler, I. V., Nielsen, T. F. D., and Tegner, C. (2011). Silicate liquid immiscibility within the crystal mush: late-stage magmatic microstructures in the Skaergaard intrusion, East Greenland. *J. Petrol.* 52, 175–222. doi: 10.1093/petrology/egq077
- Humphreys, M. C. S., Menand, T., Blundy, J. D., and Klimm, K. (2008). Magma ascent rates in explosive eruptions: constraints from H<sub>2</sub>O diffusion in melt inclusions. *Earth Planet. Sci. Lett.* 270, 25–40. doi: 10.1016/j.epsl.2008.02.041
- Jarosewich, E., Gooley, R., and Husler, J. (1987). Chromium augite—a new microprobe reference sample. *Geostand. Geoanal. Res.* 11, 197–198. doi: 10.1111/j.1751-908X.1987.tb00027.x
- Jarosewich, E., Nelen, J. A., and Norberg, J. A. (1980). Reference samples for electron microprobe analysis. *Geostand. Newslett.* 4, 43–47. doi: 10.1111/j.1751-908X.1980.tb00273.x
- Katz, R. F., Spiegelman, M., and Langmuir, C. H. (2003). A new parameterization of hydrous mantle melting. *Geochem. Geophys. Geosyst.* 4, 1–19. doi: 10.1029/2002GC000433
- Kerr, R. C. (1995). Convective crystal dissolution. *Contrib. Mineral. Petrol.* 121, 237–246. doi: 10.1007/BF02688239
- La Spina, G., Burton, M., and de' Michieli Vitturi, M. (2015). Temperature evolution during magma ascent in basaltic effusive eruptions: a numerical application to Stromboli volcano. *Earth Planet. Sci. Lett.* 426, 89–100. doi: 10.1016/j.epsl.2015.06.015
- La Spina, G., Clarke, A. B., de' Michieli Vitturi, M., Burton, M., Allison, C. M., Roggensack, K., et al. (2019). Conduit dynamics of highly explosive basaltic eruptions: the 1085 CE sunset crater sub-Plinian events. *J. Volcanol. Geotherm. Res.* 387:106658. doi: 10.1016/j.jvolgeores.2019.08.001
- Liang, Y., Richter, F. M., and Watson, E. B. (1996). Diffusion in silicate melts: II. multicomponent diffusion in CaO-Al<sub>2</sub>O<sub>3</sub>-SiO<sub>2</sub> at 1500°C and 1 GPa. *Geochim. Cosmochim. Acta* 60, 5021–5035. doi: 10.1016/S0016-7037(96)00352-3
- Lindsley, D. H., and Andersen, D. J. (1983). A two-pyroxene thermometer. *J. Geophys. Res.* 88, A887–A906. doi: 10.1029/JB088iS02p0A887
- Lloyd, A. S., Ruprecht, P., Hauri, E. H., Rose, W., Gonnermann, H. M., and Plank, T. A. (2014). NanoSIMS results from olivine-hosted melt embayments: magma ascent rate during explosive basaltic eruptions. *J. Volcanol. Geotherm. Res.* 283, 1–18. doi: 10.1016/j.jvolgeores.2014.06.002
- MacLennan, J. (2008). Concurrent mixing and cooling of melts under Iceland. *J. Petrol.* 49, 1931–1953. doi: 10.1093/petrology/egn052
- MacLennan, J. (2019). Mafic tiers and transient mushes: evidence from Iceland. *Philos. Trans. R. Soc. A* 377:20180021. doi: 10.1098/rsta.2018.0021
- MacLennan, J., Gaetani, G. A., Hartley, M. E., Neave, D. A., and Wimpenny, B. (2012). "Petrological constraints on the crustal structure under rift zones," in *AGU Fall Meeting Abstracts* (San Francisco, CA), T41G.
- MacLennan, J., McKenzie, D., Grönvold, K., Shimizu, N., Eiler, J. M., and Kitchen, N. (2003a). Melt mixing and crystallization under Theistareykir, northeast Iceland. *Geochem. Geophys. Geosyst.* 4, 1–40. doi: 10.1029/2003GC000558
- MacLennan, J., McKenzie, D., Grönvold, K., and Slater, L. (2001). Crustal accretion under Northern Iceland. *Earth Planet. Sci. Lett.* 191, 295–310. doi: 10.1016/S0012-821X(01)00420-4
- MacLennan, J., McKenzie, D., Hilton, F., Grönvold, K., and Shimizu, N. (2003b). Geochemical variability in a single flow from northern Iceland. *J. Geophys. Res.* 108, 1–21. doi: 10.1029/2000JB000142
- Magee, C., Stevenson, C. T. E., Ebmeier, S. K., Keir, D., Hammond, J. O. S., Gottsmann, J. H., et al. (2018). Magma plumbing systems: a geophysical perspective. *J. Petrol.* 59, 1217–1251. doi: 10.1093/petrology/egy064
- Marsh, B. D. (2004). A magmatic mush column Rosetta stone: the McMurdo dry valleys of Antarctica. *EOS Trans. Am. Geophys. Union* 85, 497–508. doi: 10.1029/2004EO470001
- Master, L. G. (2002). Insights into volcanic conduit flow from an open-source numerical model. *Geochem. Geophys. Geosyst.* 3, 1–18. doi: 10.1029/2001GC000192
- Michael, P. J. (1988). The concentration, behavior and storage of H<sub>2</sub>O in the suboceanic upper mantle: implications for mantle metasomatism. *Geochim. Cosmochim. Acta* 52, 555–566. doi: 10.1016/0016-7037(88)90110-X
- Miller, W. G. R., MacLennan, J., Shorttle, O., Gaetani, G. A., Le Roux, V., and Klein, F. (2019). Estimating the carbon content of the deep mantle with Icelandic melt inclusions. *Earth Planet. Sci. Lett.* 523:115699. doi: 10.1016/j.epsl.2019.07.002
- Mollo, S., Del Gaudio, P., Ventura, G., Iezzi, G., and Scarlato, P. (2010). Dependence of clinopyroxene composition on cooling rate in basaltic magmas: implications for thermobarometry. *Lithos* 118, 302–312. doi: 10.1016/j.lithos.2010.05.006
- Mollo, S., Giacomoni, P. P., Andronico, D., and Scarlato, P. (2015). Clinopyroxene and titanomagnetite cation redistributions at Mt. Etna volcano (Sicily, Italy): footprints of the final solidification history of lava fountains and lava flows. *Chem. Geol.* 406, 45–54. doi: 10.1016/j.chemgeo.2015.04.017
- Mutch, E. J. F., MacLennan, J., Holland, T. J. B., and Buisman, I. (2019a). Millennial storage of near-Moho magma. *Science* 264, 260–264. doi: 10.1126/science.aax4092
- Mutch, E. J. F., MacLennan, J., Shorttle, O., Edmonds, M., and Rudge, J. F. (2019b). Rapid transcrustal magma movement under Iceland. *Nat. Geosci.* 12, 569–574. doi: 10.1038/s41561-019-0376-9
- Namiki, A., and Manga, M. (2006). Influence of decompression rate on the expansion velocity and expansion style of bubbly fluids. *J. Geophys. Res. Solid Earth* 111, 1–17. doi: 10.1029/2005JB004132
- Namiki, A., and Manga, M. (2008). Transition between fragmentation and permeable outgassing of low viscosity magmas. *J. Volcanol. Geotherm. Res.* 169, 48–60. doi: 10.1016/j.jvolgeores.2007.07.020
- Neave, D. A., Bali, E., Gufinnsson, G. H., Halldórsson, S. A., Kahl, M., Schmidt, A.-S., et al. (2019a). Clinopyroxene-liquid equilibria and geothermobarometry in natural and experimental tholeiites: the 2014–2015 Holuhraun eruption, Iceland. *J. Petrol.* 60, 1653–1680. doi: 10.1093/petrology/egz042
- Neave, D. A., Buisman, I., and MacLennan, J. (2017a). Continuous mush disaggregation during the long-lasting Laki fissure eruption, Iceland. *Am. Mineral.* 102, 2007–2021. doi: 10.2138/am-2017-6015CCBY
- Neave, D. A., Hartley, M. E., MacLennan, J., Edmonds, M., and Thordarson, T. (2017b). Volatile and light lithophile elements in high-anorthite plagioclase-hosted melt inclusions from Iceland. *Geochim. Cosmochim. Acta* 205, 100–118. doi: 10.1016/j.gca.2017.02.009
- Neave, D. A., MacLennan, J., Hartley, M. E., Edmonds, M., and Thordarson, T. (2014). Crystal storage and transfer in basaltic systems: the Skuggaföll eruption, Iceland. *J. Petrol.* 55, 2311–2346. doi: 10.1093/petrology/egu058
- Neave, D. A., Namur, O., Shorttle, O., and Holtz, F. (2019b). Magmatic evolution biases basaltic records of mantle chemistry towards melts from recycled sources. *Earth Planet. Sci. Lett.* 520, 199–211. doi: 10.1016/j.epsl.2019.06.003
- Neave, D. A., and Putirka, K. D. (2017). A new clinopyroxene-liquid barometer, and implications for magma storage pressures under Icelandic rift zones. *Am. Mineral.* 102, 777–794. doi: 10.2138/am-2017-5968
- Newcombe, M. E., Plank, T., Barth, A., Asimow, P., and Hauri, E. (2020). Water-olivine magma ascent chronometry: every crystal is a clock. *J. Volcanol. Geotherm. Res.* 398:106872. doi: 10.1016/j.jvolgeores.2020.106872
- O'Donnell, T., and Presnall, D. C. (1980). Chemical variations of the glass and mineral phases in basalts dredged from 25–30°N along the Mid-Atlantic Ridge. *Am. J. Sci.* 280, 845–868.
- Pearson, D. G., Canil, D., and Shirey, S. B. (2003). Mantle samples included in volcanic rocks: xenoliths and diamonds. *Treat. Geochem.* 2–9, 171–275. doi: 10.1016/B0-08-043751-6/02005-3
- Peslier, A. H., Bizimis, M., and Matney, M. (2015). Water disequilibrium in olivines from Hawaiian peridotites: recent metasomatism, H diffusion and magma ascent rates. *Geochim. Cosmochim. Acta* 154, 98–117. doi: 10.1016/j.gca.2015.01.030
- Pirrie, D., Butcher, A. R., Power, M. R., Gottlieb, P., and Miller, G. L. (2004). Rapid quantitative mineral and phase analysis using automated scanning electron

- microscopy (QemSCAN); potential applications in forensic geoscience. *Geol. Soc. Lond. Spec. Publ.* 232, 123–136. doi: 10.1144/GSL.SP.2004.232.01.12
- Presnall, D. C., Dixon, S. A., Dixon, J. R., O'Donnell, T. H., Brenner, N. L., Schrock, R. L., et al. (1978). Liquidus phase relations on the join diopside-forsterite-anorthite from 1 atm to 20 kbar: their bearing on the generation and crystallization of basaltic magma. *Contrib. Mineral. Petrol.* 66, 203–220. doi: 10.1007/BF00372159
- Putirka, K. D. (2008). Thermometers and barometers for volcanic systems. *Rev. Mineral. Geochem.* 69, 61–120. doi: 10.2138/rmg.2008.69.3
- Putirka, K. D., Johnson, M., Kinzler, R. J., Longhi, J., and Walker, D. (1996). Thermobarometry of mafic igneous rocks based on clinopyroxene-liquid equilibria, 0–30 kbar. *Contrib. Mineral. Petrol.* 123, 92–108. doi: 10.1007/s004100050145
- R Development Core Team (2016). *R: A Language and Environment for Statistical Computing*. Vienna: R Foundation for Statistical Computing.
- Rudnick, R. L. (1992). Xenoliths—samples of the lower continental crust. *Contin. Lower Crust* 23, 269–316.
- Ruprecht, P., and Plank, T. A. (2013). Feeding andesitic eruptions with a high-speed connection from the mantle. *Nature* 500, 68–72. doi: 10.1038/nature12342
- Rutherford, M. J. (2008). Magma ascent rates. *Rev. Mineral. Geochem.* 69, 241–271. doi: 10.2138/rmg.2008.69.7
- Saal, A. E., Hauri, E. H., Langmuir, C. H., and Perfit, M. R. (2002). Vapour undersaturation in primitive mid-ocean-ridge basalt and the volatile content of earth's upper mantle. *Nature* 419, 451–455. doi: 10.1038/nature01073
- Scarlato, P., Mollo, S., Del Bello, E., von Quadt, A., Brown, R. J., Gutierrez, E., et al. (2017). The 2013 eruption of Chaparrastique volcano (El Salvador): effects of magma storage, mixing, and decompression. *Chem. Geol.* 448, 110–122. doi: 10.1016/j.chemgeo.2016.11.015
- Shea, T., Lynn, K. J., and Garcia, M. O. (2015). Cracking the olivine zoning code: distinguishing between crystal growth and diffusion. *Geology* 43, 935–938. doi: 10.1130/G37082.1
- Sigurdsson, I. A., Steinhórrson, S., and Grönvold, K. (2000). Calcium-rich melt inclusions in Cr-spinels from Borgarhraun, northern Iceland. *Earth Planet. Sci. Lett.* 183, 15–26. doi: 10.1016/S0012-821X(00)00269-7
- Smith, P. M., and Asimow, P. D. (2005). Adibat-1ph: a new public front-end to the MELTS, pMELTS, and pHMELTS models. *Geochem. Geophys. Geosyst.* 6, 1–8. doi: 10.1029/2004GC000816
- Sparks, R. S. J., Annen, C., Blundy, J. D., Cashman, K. V., Rust, A. C., and Jackson, M. D. (2019). Formation and dynamics of magma reservoirs. *Philos. Trans. R. Soc. A* 377:20180019. doi: 10.1098/rsta.2018.0019
- Sparks, R. S. J., and Cashman, K. V. (2017). Dynamic magma systems: implications for forecasting volcanic activity. *Elements* 13, 35–40. doi: 10.2113/gselements.13.1.35
- Staples, R. K., White, R. S., Brandsdóttir, B., Menke, W., Maguire, P. K. H., and McBride, J. H. (1997). Färoe-Iceland ridge experiment 1. Crustal structure of northeastern Iceland. *J. Geophys. Res. Solid Earth* 102, 7849–7866. doi: 10.1029/96JB03911
- Streck, M. J. (2008). Mineral textures and zoning as evidence for open system processes. *Rev. Mineral. Geochem.* 69, 595–622. doi: 10.2138/rmg.2008.69.15
- Sugawara, T. (2000). Empirical relationships between temperature, pressure, and MgO content in olivine and pyroxene saturated liquid. *J. Geophys. Res.* 105, 8457–8472. doi: 10.1029/2000JB900010
- Tarasewicz, J., Brandsdóttir, B., White, R. S., Hensch, M., and Thorbjarnardóttir, B. (2012). Using microearthquakes to track repeated magma intrusions beneath the Eyjafjallajökull stratovolcano, Iceland. *J. Geophys. Res. Solid Earth* 117, 1–13. doi: 10.1029/2011JB008751
- Thompson, G., Bryan, W. B., and Melson, W. G. (1980). Geological and geophysical investigation of the mid-Cayman rise spreading center: geochemical variation and petrogenesis of basalt glasses. *J. Geol.* 88, 41–55. doi: 10.1086/628472
- Thompson, R. N. (1974). Some high-pressure pyroxenes. *Mineral. Mag.* 39, 768–787. doi: 10.1180/minmag.1974.039.307.04
- Trønnes, R. G. (1990). Basaltic melt evolution of the Hengill volcanic system, SW Iceland, and evidence for clinopyroxene assimilation in primitive tholeiitic magmas. *J. Geophys. Res. Solid Earth* 95, 15893–15910. doi: 10.1029/JB095iB10p15893
- Tsuchiyama, A. (1986). Melting and dissolution kinetics: application to partial melting and dissolution of xenoliths. *J. Geophys. Res.* 91:9395. doi: 10.1029/JB091iB09p09395
- Welsch, B., Hammer, J. E., Baronnet, A., Jacob, S., Hellebrand, E., and Sinton, J. M. (2016). Clinopyroxene in postshield Haleakala ankaramite 2. Texture, compositional zoning, and supersaturation in the magma. *Contrib. Mineral. Petrol.* 171:6. doi: 10.1007/s00410-015-1213-9
- White, R. S., Drew, J., Martens, H. R., Key, J., Soosalu, H., and Jakobsdóttir, S. S. (2011). Dynamics of dyke intrusion in the mid-crust of Iceland. *Earth Planet. Sci. Lett.* 304, 300–312. doi: 10.1016/j.epsl.2011.02.038
- Wilson, L., and Head, J. W. (1981). Ascent and eruption of basaltic magma on the earth and moon. *J. Geophys. Res. Solid Earth* 86, 2971–3001. doi: 10.1029/JB086iB04p02971
- Winpenny, B., and MacLennan, J. (2011). A partial record of mixing of mantle melts preserved in Icelandic phenocrysts. *J. Petrol.* 52, 1791–1812. doi: 10.1093/ptrology/egr031
- Woods, A. W., and Koyaguchi, T. (1994). Transitions between explosive and effusive eruptions of silicic magmas. *Nature* 370, 641–644. doi: 10.1038/370641a0
- Wright, H. M. N., Cashman, K. V., Mothes, P. A., Hall, M. L., Ruiz, A. G., and Le Pennec, J. L. (2012). Estimating rates of decompression from textures of erupted ash particles produced by 1999–2006 eruptions of Tungurahua volcano, Ecuador. *Geology* 40, 619–622. doi: 10.1130/G32948.1
- Yang, H.-J., Kinzler, R. J., and Grove, T. L. (1996). Experiments and models of anhydrous, basaltic olivine-plagioclase-augite saturated melts from 0.001 to 10 kbar. *Contrib. Mineral. Petrol.* 124, 1–18. doi: 10.1007/s004100050169
- Yu, Y., Zhang, Y., Chen, Y., and Xu, Z. (2016). Kinetics of anorthite dissolution in basaltic melt. *Geochim. Cosmochim. Acta* 179, 257–274. doi: 10.1016/j.gca.2016.02.002
- Zhang, X., Ganguly, J., and Ito, M. (2010a). Ca-Mg diffusion in diopside: tracer and chemical inter-diffusion coefficients. *Contrib. Mineral. Petrol.* 159, 175–186. doi: 10.1007/s00410-009-0422-5
- Zhang, Y., Ni, H., and Chen, Y. (2010b). Diffusion data in silicate melts. *Rev. Mineral. Geochem.* 72, 311–408. doi: 10.2138/rmg.2010.72.8
- Zhang, Y., Walker, D., and Lesher, C. E. (1989). Diffusive crystal dissolution. *Contrib. Mineral. Petrol.* 102, 492–513. doi: 10.1007/BF00371090
- Zhang, Y., and Xu, Z. (2003). Kinetics of convective crystal dissolution and melting, with applications to methane hydrate dissolution and dissociation in seawater. *Earth Planet. Sci. Lett.* 213, 133–148. doi: 10.1016/S0012-821X(03)00297-8

**Conflict of Interest:** The authors declare that the research was conducted in the absence of any commercial or financial relationships that could be construed as a potential conflict of interest.

Copyright © 2020 Neave and MacLennan. This is an open-access article distributed under the terms of the Creative Commons Attribution License (CC BY). The use, distribution or reproduction in other forums is permitted, provided the original author(s) and the copyright owner(s) are credited and that the original publication in this journal is cited, in accordance with accepted academic practice. No use, distribution or reproduction is permitted which does not comply with these terms.